ORIGINAL PAPER

Toward noise certification during design: airframe noise simulations for full-scale, complete aircraft

Mehdi R. Khorrami[1,3] · **Ehab Fares**[2,4]

Abstract

An overview of a recent, NASA-sponsored effort to substantially advance simulation-based airframe noise prediction is presented. An accurate characterization of this component of aircraft noise requires a high-fidelity representation of the finer geometrical details associated with the landing gear and wing high-lift devices, such as slats and flaps, which constitute major noise sources. To achieve this ambitious goal, a systematic approach was followed to extend our current state-of-the-art computational tools to a full-scale, complete aircraft in landing configuration within a realistic flight environment. The work involved several phases: high-fidelity, large-scale, unsteady flow simulations; model-scale experiments in ground-based facilities; and farfield noise prediction for a full-scale, complete aircraft. The comprehensive aeroacoustic database generated during the course of the 6-year effort provided a wealth of relevant information for full validation and benchmarking of the advanced computational tools used in the present work. The database will also foster the development of simulation methodologies with improved predictive capabilities.

1 Introduction

Noise pollution associated with civil aircraft operations during landing and takeoff affects major population centers adjacent to airports; therefore, mitigation of aircraft noise is an important pacing item for future growth in global aviation. In a broad sense, aircraft-borne noise can be categorized as either propulsion or airframe noise. Modern high-bypass ratio turbofan engines have provided significant gains in propulsion noise reduction. As a result, during aircraft approach to landing, noise generated by the airframe is comparable to, and in most instances louder than, propulsion noise. A

good overview of primary and secondary sources of airframe noise can be found in Ref. [1]. In general, prominent sources are associated with major airframe components that are deployed during landing, i.e., the undercarriage and wing high-lift devices such as slats and flaps. The steady pace of advancement in digital technology and computational fluid dynamics (CFD) has enabled the development of high-fidelity simulation tools with accurate predictive capabilities that allow an efficient evaluation of advanced aircraft designs and viable noise reduction technologies [2–4]. Ultimately, the goal of creating such tools is to promote a paradigm shift in the design procedure from the current time-consuming and costly trial-and-error approach to a physics-based, virtual design environment whereby the aeroacoustic evaluation of a complete aircraft and its subsequent optimization can take place in an integrated, system-level fashion prior to wind tunnel or expensive flight tests.

High-fidelity, physics-based airframe noise prediction for full-scale, complete aircraft in landing configuration is a grand challenge for the aerospace community and the results summarized here constitute a promising initial attempt to meet this challenge. Such an endeavor has become possible with the advent of (1) supercomputers

---

✉ Mehdi R. Khorrami
mehdi.r.khorrami@nasa.gov

1   NASA Langley Research Center, Hampton, VA 23681, USA

2   Dassault Systemes Deutschland GmbH, Curiestrasse 4, 70563 Stuttgart, Germany

3   Computational AeroSciences Branch, Hampton, USA

4   SIMULIA A&D, Stuttgart, Germany

with thousands of cores; (2) computational algorithms able to efficiently distribute billions of calculations over thousands of processors; (3) agile surface preparation and volume discretization software that permit the rapid creation of meshes around extremely complex configurations; and (4) highly parallelizable equations that statistically describe the behavior of fluid media, such as the lattice Boltzmann method (LBM). The primary software suite used during the multi-year effort described in this overview possesses the last three characteristics. Certainly, advocacy of the LBM as the only approach for airframe noise prediction is not the purpose here. In fact, the first author led a targeted effort where a standard, unstructured Navier–Stokes flow solver was applied to configurations similar to those addressed in this article [5, 6]. However, until the generation of unstructured volume grids around configurations of extreme geometric complexity becomes efficient enough so that a family of meshes with successively finer resolutions can be created with relative ease, the execution of large-scale, unsteady simulations with Navier–Stokes solvers will be fraught with numerous challenges, paramount among them the difficulty to achieve a grid-independent solution and the prohibitive amounts of time and manpower needed to do so.

The present overview relies entirely on NASA-sponsored research conducted during the past 6 years, an effort with which we are intimately familiar. Omission of other potential contributions to this summary has not been intentional. We were unable to find, in the open literature, other examples of airframe noise simulations for complete aircraft in landing configuration, either for full- or model-scale. We do not suggest that the state of the art in airframe noise prediction is at a stage where the type of high-fidelity, high resolution simulations presented in this overview are, or can be, routinely performed during aircraft design cycles. Rather, as the thought-provoking title of this article implies, our intent is to highlight the predictive capabilities of tools that are available to the airframe noise community and have the potential to be ubiquitous as computers become more powerful and the cost per simulation is lowered in the coming years.

1.1 On the importance of geometric detail

Accurate prediction of airframe noise for full-scale, complete aircraft during landing is exceptionally difficult because of various inherent characteristics: (a) extreme geometrical complexity that includes objects of disparate size and shape; (b) installation or component interaction effects; (c) unsteady, highly non-linear, turbulent flow fields containing a broad spatio-temporal range of scales; (d) Reynolds number (Re) effects; and (e) capture and propagation of broadband noise to the far field. The geometric complexity of major noise-producing airframe components can be observed in the images of Fig. 1. Note from Fig. 1a that the main landing gear (MLG) of a large civil transport is composed of many subsystems with elements of various sizes and shapes. A successful simulation of the near-field unsteady flow (the noise sources) for such a geometry must address these challenges: resolution of the time-dependent flow associated with the many gear structures (self-noise), proper convection and preservation of the wakes generated by the various subsystem components, and accurate capture of wake impingement on downstream structures (interaction noise). Also critical is the accurate resolution of near-field pressure fluctuations over broad spatial scales covering hydrodynamic fluctuations and acoustic waves with complicated diffraction and reflection patterns. The geometric fidelity required by
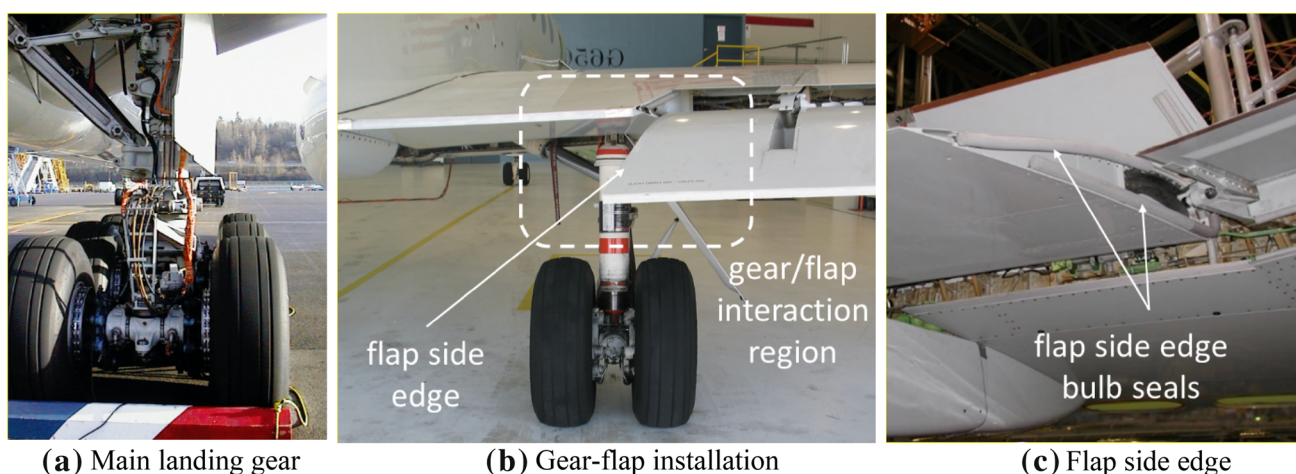

(a) Main landing gear   **(b)** Gear-flap installation   **(c)** Flap side edge

Fig. 1 Main landing gear of a large civil transport and close-up view of an aircraft flap side-edge region

simulations of this type overwhelms most grid generation processes currently in use.

Aeroacoustic studies of a realistic gear configuration in isolation provide ample knowledge on the noise generation mechanisms and dominant noise sources. However, once a landing gear is installed on an aircraft as shown in Fig. 1b, interactions among the unsteady flows developed around the gear and other components may change significantly the farfield noise signature of the gear. For many aircraft, the MLG is mounted in close proximity to the wing flap. As such, the circulation (downwash) associated with a deployed flap alters the flow upstream of the gear, while the gear wake impacts the flow field at the flap tip region. In Fig. 1c, we provide an example of a flap side-edge from an actual aircraft that is very different from the straight-edge geometry that is typically studied in model-scale experiments or simulations. As shown in the figure, the presence of a bulb seal and roller assembly make the flap tip geometry rather complex and more difficult to handle computationally. The finer geometric characteristics of full-scale airframes play a crucial role in altering the local unsteady flow, where the noise signature that propagates to the far field is generated. Elimination, or even oversimplification, of such geometric details to facilitate model-scale tests or simulations would produce a farfield noise signature that is drastically different from that associated with the full-scale aircraft. A suitable example is provided in Ref. [1], where the author demonstrates that taping various surface cutouts surrounding the slat brackets reduces the farfield noise for the component by 1.5–2.0 dB over a wide range of frequencies. Unexpected sources such as these cutouts are the most difficult to model.

Some of the key differences in requirements between aerodynamic computations (as currently practiced within the aerospace industry) and airframe noise simulations are summarized in Table 1. The use of unsteady, turbulent flow computations for full-scale aircraft is incipient within the aerodynamic design phase. Thus, we do not claim that the requirements listed in Table 1 are exhaustive. Rather, we believe that the table represents a good starting point for broader discussions within the airframe noise community on a future roadmap for conducting production-level simulations of full-scale, as-flown, aircraft geometries in landing configuration on a routine basis. This list is in accordance with the expected long-term advancement of CFD simulations within the aeronautical industry [7].

1.2 On the necessity of relevant experimental data

Computational simulations have made significant inroads as a viable, complementary tool to wind-tunnel testing for airframe noise prediction. Until recently, these complex, high-fidelity simulations were mostly confined to sub- or full-scale airframe components [8–13]. Proper extension of the simulation tools to a complete aircraft geometry required the existence of extensive sets of experimental data for a realistic configuration. The availability of such data permitted a systematic approach toward validation and benchmarking of the various stages of the selected computational methodology. The building-block experimental tests that generated the requisite aeroacoustic data were established and executed within the NASA-Gulfstream partnership on airframe noise research. Under this joint effort, a series of flight tests and model-scale experiments were conducted with a

Table 1 Simulation requirements

Aerodynamic applications	Airframe noise applications
Very accurate prediction of global flow field (lift and drag)	Accurate prediction of global flow field
Moderately accurate prediction of local flows	Very accurate prediction of local flows
Mostly steady simulation of turbulent flow	Inherently unsteady, mostly resolved turbulent flow
Finer geometric details are of secondary importance	Geometric details very important (slat tracks, gear brake assembly, etc.)
Design point is usually cruise	Design point is always landing
Off-design (landing)	Landing
Accurate prediction of stall is critical	Accurate prediction of stall critical for noise reduction concept validation
Landing gear generally ignored	Landing gear is essential
Spatial/temporal scales not important	Vast range of spatial/temporal scales (broadband noise)
Focus on hydrodynamic near-field	Hydrodynamic near- and acoustic farfield very important Propagation of broadband noise over large distances
Compressibility effects at low speed/off-design not important	Compressibility is important for proper noise characterization
Result is typically averaged quantities and averaged flow field	Unsteady high-frequency data are collected for subsequent post processing
Numerical resolution determined by acceptable grid convergence of global flow field	Numerical resolution determined by high-frequency requirements
Simulation time determined by acceptable flow convergence	Simulation time determined by statistical convergence and lowest frequency resolution

Gulfstream aircraft as the baseline configuration. An 18% scale, semispan replica of the chosen aircraft was designed and fabricated specifically to conduct airframe noise studies and evaluate noise reduction concepts for mitigating landing gear, flap, and gear–flap interaction noise. Aeroacoustic testing of the semispan model was performed through carefully planned entries in the NASA Langley Research Center (LaRC) 14- by 22-Foot Subsonic Wind Tunnel (14×22). The initial entry, completed in November 2010, focused on acquiring global forces (lift and drag) and measurements of steady and unsteady surface pressures. Detailed accounts of that entry and the processed aerodynamic data are given in Refs. [14, 15]. The second 14×22 tunnel entry was executed in two segments. The first segment was dedicated to simultaneous acoustic and surface pressure measurements [16, 17], while the second segment was devoted to off-surface flow measurements for the nominal aircraft landing configuration [18]. The sub-scale aeroacoustic measurements complemented the acoustic data acquired during a flight-test campaign executed in 2006 with the same Gulfstream aircraft as the testbed [19].

1.3 Organization of overview

The present paper is organized as follows. Descriptions of the model- and full-scale aircraft geometries used for aeroacoustic simulations are given in Sect. 2. In Sect. 3, a brief account of the selected computational approach is provided and the most pertinent aspects of the methodology highlighted. Sample computational results from the model-scale simulations are presented in Sect. 4, where spatial resolution effects and comparison with near-field flow and far-field acoustic measurements are discussed. Also presented in this section are the outcomes from simulations that were undertaken to determine *Re* and Mach number (*M*) effects on farfield acoustic behavior. Section 5 discusses simulations obtained for the full-scale Gulfstream aircraft in landing configuration and comparisons with available measurements. Also, an example of the effects of geometrical detail

on farfield noise signature and the computational challenges posed by such detail are discussed in this section. Several of the figures presented in Sects. 4 and 5 do not contain values on the ordinate axis. This omission is necessary to guard the proprietary nature of select aerodynamic and acoustic data. A summary of the computational effort aimed at extending simulation-based airframe noise prediction to a complete aircraft in landing configuration is provided in Sect. 6. The paper concludes with Sect. 7, where anticipated future work with the current methodology is discussed briefly.
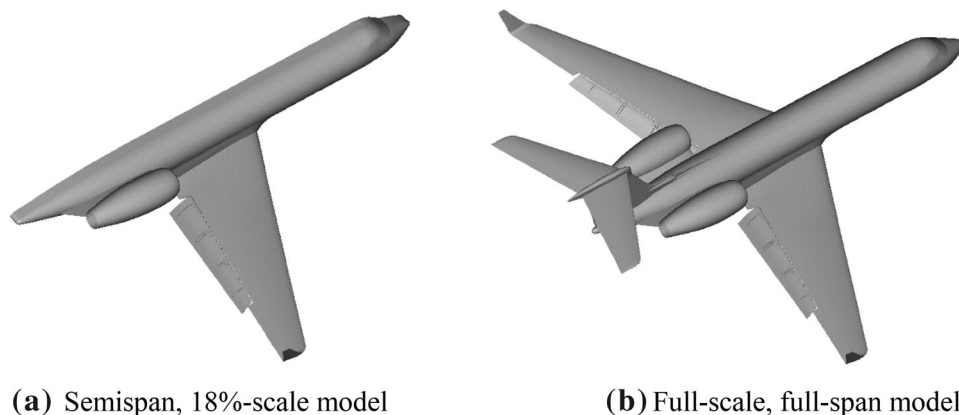
2 Simulated aircraft geometries

The simulated geometry corresponds to a Gulfstream aircraft that was used during the NASA-Gulfstream joint airframe noise flight test conducted in 2006 [19]. Two high-fidelity versions of this geometry were used to perform the simulations presented here: an 18%-scale, semispan reproduction that was used for an extensive study of flap and landing gear noise sources and corresponding noise mitigation concepts [14–18, 20]; and a full-scale, full-span representation of the aircraft. These two versions are depicted in Fig. 2 and described in the following paragraphs.
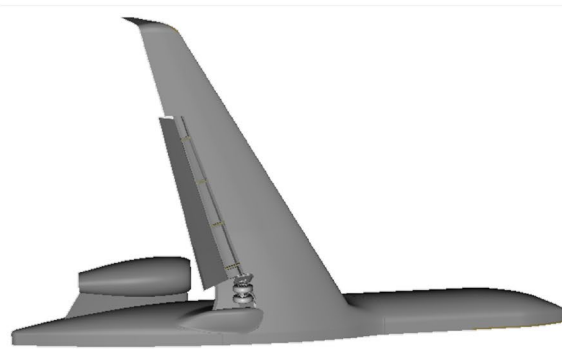
2.1 Model-scale geometry

The 18%-scale geometry consists of a fuselage, wing, flap, flow-through nacelle, pylon, and MLG (Fig. 3). We note here that the Gulfstream aircraft does not have leading edge slats. A full description of this model, including the surface distribution of steady pressure ports and unsteady transducers on various components, is provided in Refs. [14, 15]. In building the model, special care was taken to replicate the airframe finer details that were deemed important to local flow unsteadiness and thus the noise generation mechanisms. Nevertheless, the geometry of certain components (e.g., flap bracket assemblies, cavity and bulb-seal assembly at flap outboard tip) was altered to maintain the proper stress and

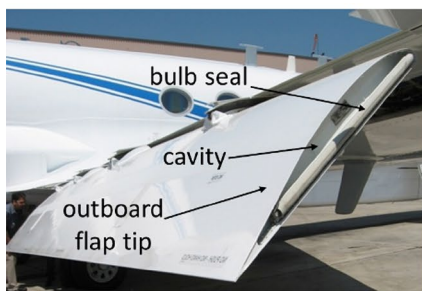**Fig. 2** Simulated aircraft geometries

(a) Semispan, 18%-scale model   **(b)** Full-scale, full-span model

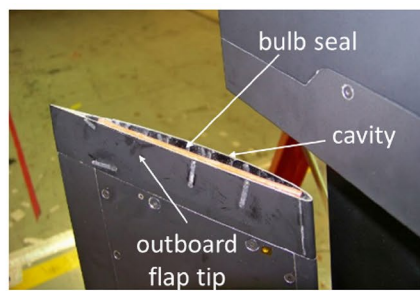**(a)** Installed in NASA LaRC 14×22 wind tunnel   **(b)** CAD model used in simulations
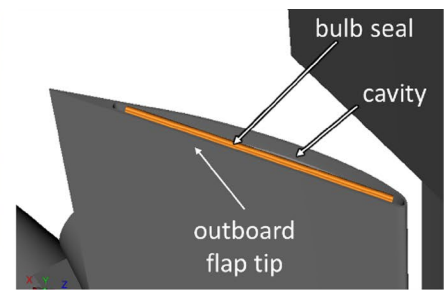
Fig. 3 Subscale (18%) semispan model of a Gulfstream aircraft

(a) Full-scale aircraft   **(b)** Tested 18%-scale model   **(c)** Simulated 18%-scale CAD model

Fig. 4 Outboard flap tip geometry of Gulfstream aircraft

load requirements associated with the aerodynamic forces produced by the model and to resolve difficulties in reproducing already small features at 18%-scale. An example of the physical fidelity of the model is presented in Fig. 4, where the cavity and bulb seal located at the flap outboard tip of an actual aircraft is compared with the 18%-scale model representation. For the sub-scale simulations, the "as-built", tunnel-tested aircraft model was used. Configurations comprising the flap deflected 39° with and without MLG deployed were identified as the baseline cases used to evaluate the noise prediction capabilities of the chosen computational strategy.

2.2 Full-scale geometry

For full-scale, complete aircraft simulations, the CAD geometry was developed using a full-scale version of the 18%-scale model fuselage, wing, and flow-through nacelle; the flaps, including their complex bracket/track system, as well as the vertical and horizontal tails, were developed using as-flown, full-scale geometry files furnished by the Gulfstream Aerospace Corporation (GAC). The MLG, including the wheel cavity, was developed from the original full-scale

geometry files containing the finer details of the gear as deployed on the actual aircraft. The larger structures residing within the wheel well that could potentially alter the cavity volume were also included. Because the gear cavity extends across the fuselage, the full aircraft span had to be considered in the simulations. The computational cost and resources required for each simulated full-scale configuration were significantly higher than those used for the 18%-scale, semispan model simulations [21–23] mainly due to increased *Re*, consideration of the full-span geometry, and inclusion of aircraft finer details. For full-scale simulations, a configuration of 39° flap deflection with and without MLG deployed (Fig. 5a) was used. We will also present our latest results for the more complete landing configuration that includes the nose landing gear as shown in Fig. 5b.

3 Computational methodology

A key decision at the beginning of our simulation effort was the choice of computational approach. Given the status and anticipated growth in computational power, application of methods such as direct numerical simulation

(a) Flaps deflected 39° with main gear deployed; left image 2006 flight test, right image simulated CAD model

(b) Flaps deflected 39° with main and nose gears deployed; left image 2006 flight test, right image simulated CAD model

Fig. 5 Baseline configurations for full-scale Gulfstream aircraft

(DNS), large eddy simulation (LES), or even the considerably less resource-intensive wall modeled large eddy simulation (WMLES) to a complete aircraft for realistic *Re* is not feasible even on the most powerful computer cluster available today. Recently developed hybrid methods for turbulent flow computations, such as delayed detached eddy simulation (DDES) [24] or scale adaptive simulation (SAS) [25] and their many variants, facilitated the extension of high-fidelity unsteady simulations to more complex geometries while keeping execution within reasonable cost and time. The selection of computational methodology was made after careful consideration of the challenges and pitfalls that are associated with such complex simulations. Foremost among the attributes considered were (a) the capability to handle extremely complex geometries, (b) ease of grid generation and convenient mesh refinement to ascertain the spatial accuracy and grid convergence behavior of the solutions, (c) low dispersion and dissipation properties of the numerical scheme, and (d) fast and efficient execution of large-scale, time–accurate computations on massively-parallel platforms. Thus, based on the knowledge and experience gained from previous aeroacoustic simulations of an isolated nose landing gear for a Gulfstream aircraft and other relevant configurations [8–13], the present full-scale, complete aircraft, airframe noise prediction effort was pursued via application of the Lattice Boltzmann-Very Large Eddy Simulation (LB-VLES) approach within the Exa Corporation PowerFLOW® solver [26–29]. The lattice Boltzmann formulation is solved on Cartesian meshes that are generated automatically within PowerFLOW® for any geometrically complex shape. This greatly simplifies the labor-intensive volume meshing

step usually associated with other approaches. Gridding strategy, overall mesh distribution, and arrangement of the variable resolution (VR) regions for various grids were described in Refs. [21–23, 30, 31]. For every simulation, a grid resolution study was performed with additional medium and coarse meshes, comprised of globally larger Cartesian volume element (voxel) sizes of factor 1.5 and 2.25, respectively. Sample slices of the fine-resolution grid are shown in Fig. 6.

The majority of simulations were performed for free air. All aircraft surfaces were modeled with no slip boundary conditions and sponge layer zones with exponentially increasing viscosity towards the free-field boundary were included in the far field to dampen acoustic wave reflection. All simulations were initialized with freestream conditions to ensure comparability of temporal evolution. Each simulation proceeded with an explicit physical time step (on the order of a few microseconds) for 30–40 flow passes along the mean aerodynamic chord to allow settling of the flow before the sampling phase of the solution was initiated. A sampling rate of approximately 10^5 Hz was used during the simulations. An acoustic analogy approach based on the Ffowcs Williams and Hawkings (FWH) formulation [32] was employed to propagate the computed near-field fluctuations to the far field as described in Refs. [32–34].

4 Model-scale simulation results

The 18%-scale semispan model was used as the initial step to demonstrate the viability of the selected computational approach for full-scale simulation of a complete aircraft.
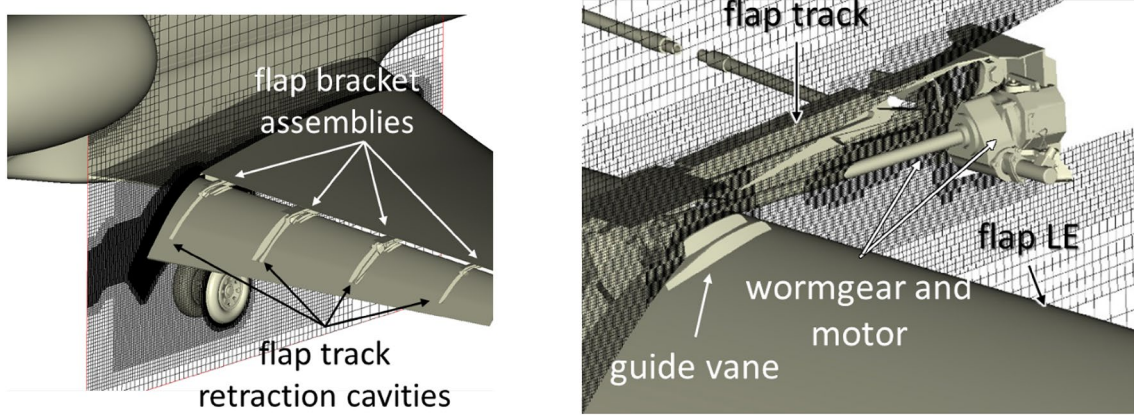
Fig. 6 Full-scale geometry and mesh at the main landing gear and inboard flap side edge (left) and flap middle bracket regions (right). Every other mesh cell is shown (from Ref. [23])

As part of the process, the extensive aeroacoustic database developed for the model from the 14×22 tunnel tests was used to conduct a thorough validation of the computed results. The 18%-scale model simulations have been documented in Refs. [21–23]. All simulations were obtained for a free-air setup at a freestream M of 0.2. The corresponding unit Re is 1.33×10^6 per foot (4.40×10^6 per meter), resulting in Re of 3.40×10^6 based on the 18%-scale model mean aerodynamic chord of 30.8 in (0.782 m). For demonstration purposes, we limit ourselves to representative sample results to highlight the predictive capability and level of accuracy achieved with the current computational methodology.

The 18%-scale model provided a unique opportunity to investigate, for the first time, gear-flap (component) interaction in a system-level basis under relevant conditions. Although the simulated flap geometry is very complex, including several brackets and tracks, worm gears, and guide vanes, the major sources of flow unsteadiness are located in the vicinity of the two flap side edges and the MLG. The latter impacts the overall aerodynamic performance of the aircraft by increasing drag. Because the MLG is located under the wing, its wake is convected past the inboard portion of the flap, where a significant localized effect is expected. A snapshot of the vorticity field in the region containing the gear and inboard flap tip is presented in Fig. 7. In the left image, the separated shear layers at the flap tips are rapidly deformed by Kelvin–Helmholtz instabilities, resulting in the formation of numerous vortex filaments of different sizes and shapes. Roll-up of the deformed shear layers produces two prominent streamwise vortices situated along the lower and upper edges of the flap tip. Downstream of the flap mid-chord, the lower side vortex begins to interact and merge with the vortex on the upper surface. Eventually, a single dominant streamwise vortex is formed. The right image also shows the presence of turbulent flow structures in the form of vortex filaments
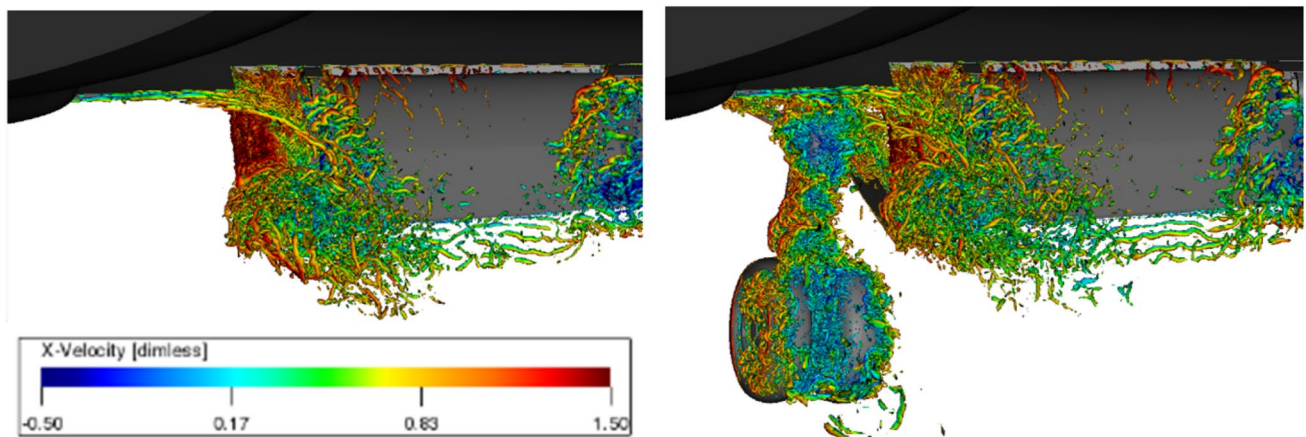

Fig. 7 Close-up view of the gear-flap interaction zone showing instantaneous vorticity field based on isosurface of λ_2 criterion (at -3000) for gear off (left) and gear on (right) configurations (from Ref. [21])

Fig. 8 Simulated total pressure contours of unsteady (top) and time-averaged (bottom) flow at the inboard flap side edge at trailing edge. Left column corresponds to gear off and right column to gear on configurations (from Ref. [21])
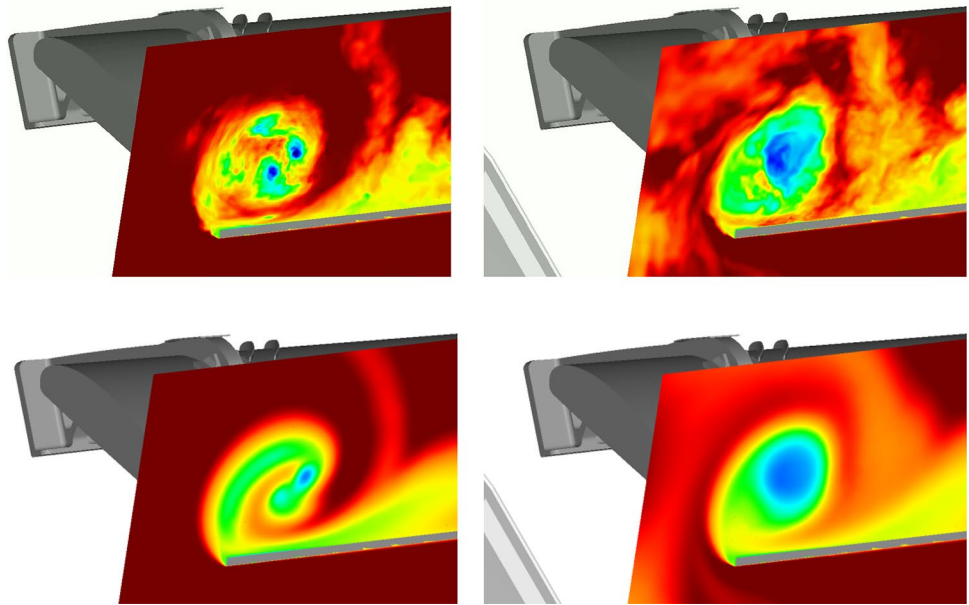
of various shapes, sizes, and strengths being shed from different gear subcomponents. These structures are the source of the broadband surface pressure fluctuations that produce the farfield noise associated with the gear. Notice that the strong interaction between the gear wake and flap inboard tip results in substantial alteration of the tip flow field.

A close-up view of the gear-flap interaction effect and the resulting alteration of the local flow at the flap inboard tip is displayed in Fig. 8. There are stark differences in the tip vortex states at the flap trailing edge between the gear off and gear on configurations. A global view of the radiated sound field produced at the flap tips for the baseline configuration without the main gear is displayed in Fig. 9a. The two-dimensional planar cut positioned at the flap mid-chord clearly shows the origin of the sound waves, which radiate spherically from both tips. The corresponding cut for the configuration with the main gear installed is presented in Fig. 9b. Note from the figure that gear

deployment does not diminish or significantly alter the sound levels nor the patterns associated with the inboard tip. However, as shown by the measurements presented in Ref. [16], deflection of the flap reduces the noise levels produced by the MLG.

4.1 Steady and unsteady surface pressures

Figure 10, reproduced from Ref. [14], shows the spanwise location and numbering of the static pressure rows on the model wing and flap. Note in Fig. 10a that the wing pressure rows extend to include the area that overlaps the stowed flap upper surface, shown in purple. This darker region represents the wing spoiler, which was treated as part of the wing for instrumentation purposes. Thus, none of the steady pressure ports on the wing or flap are common to both components.
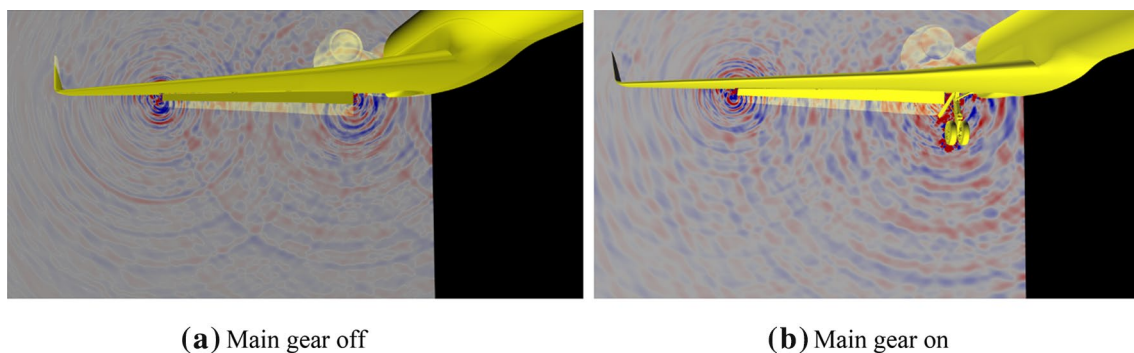

(a) Main gear off   **(b)** Main gear on

Fig. 9 Radiated sound field (dilatation field) associated with noise sources at inboard and outboard flap tips and main landing gear with planar cut at flap mid-chord (from Ref. [21])
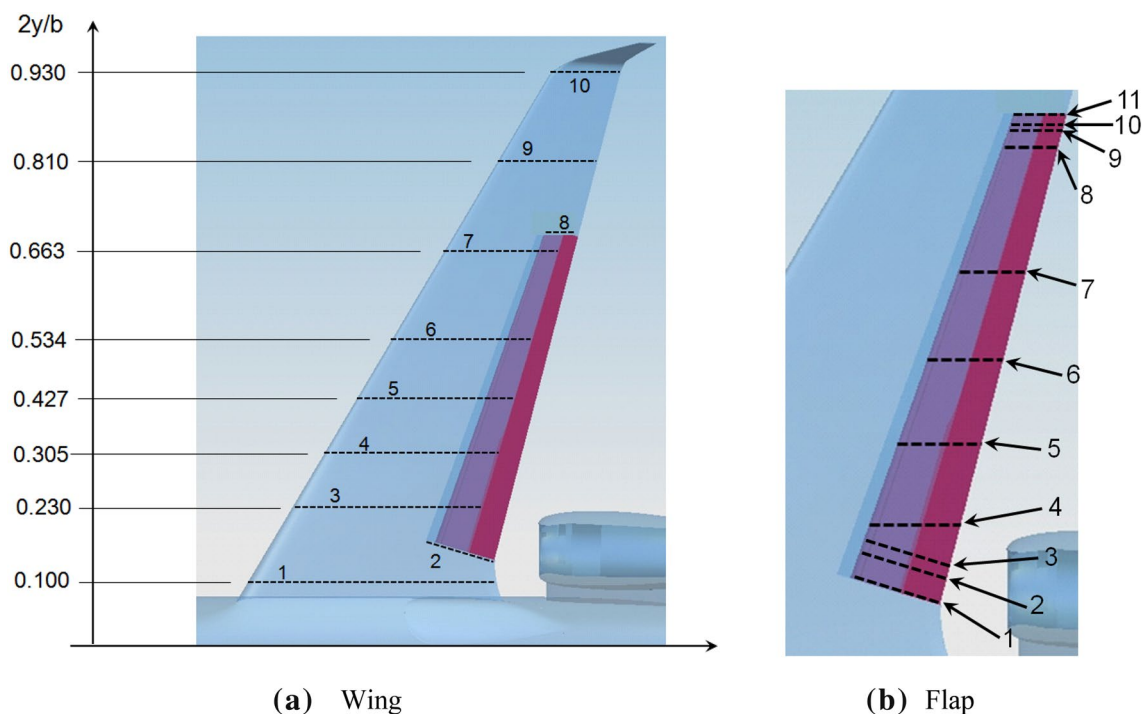
(a) Wing   **(b)** Flap

Fig. 10 Spanwise location and identification number for rows of static pressure orifices (from Ref. [14])

(a) Wing row 3   **(b)** Wing row 9
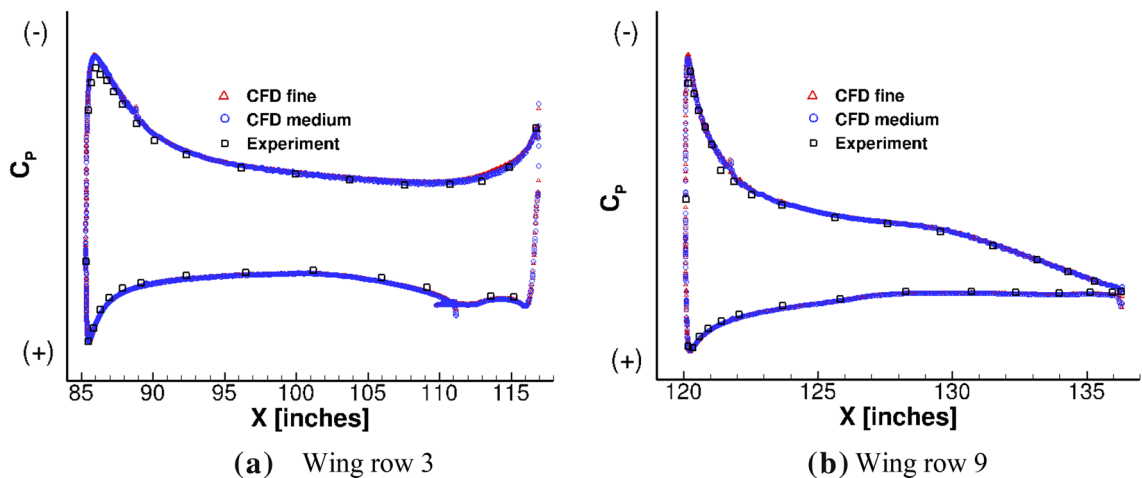
Fig. 11 Surface pressures on 18%-scale model wing (from Ref. [21])

The computed time-averaged C_p distributions for the model aircraft wing were found to be in good agreement with the measured values at all the pressure port rows. Sample C_p plots taken from Ref. [21] that compare computed and measured pressure fields at inboard and outboard rows on the wing are presented in Fig. 11 for the configuration without MLG. Results from both medium- and fine-resolution grids are displayed. Notice that nearly identical C_p values are produced by the two grids, indicating that a reasonable

degree of grid independence was attained for the steady lift produced by the wing.

Accurate simulation of the steady load at both inboard and outboard flap tips is of paramount importance to the proper prediction of edge vortex formation, development, and mitigation. Therefore, it is critical for determining the corresponding fluctuating pressure field (noise sources). Deployment of the main gear only affects the time-averaged pressure field on the lower surface of the wing (due to the gear cavity opening; row 3 in Fig. 10a) and the region in the
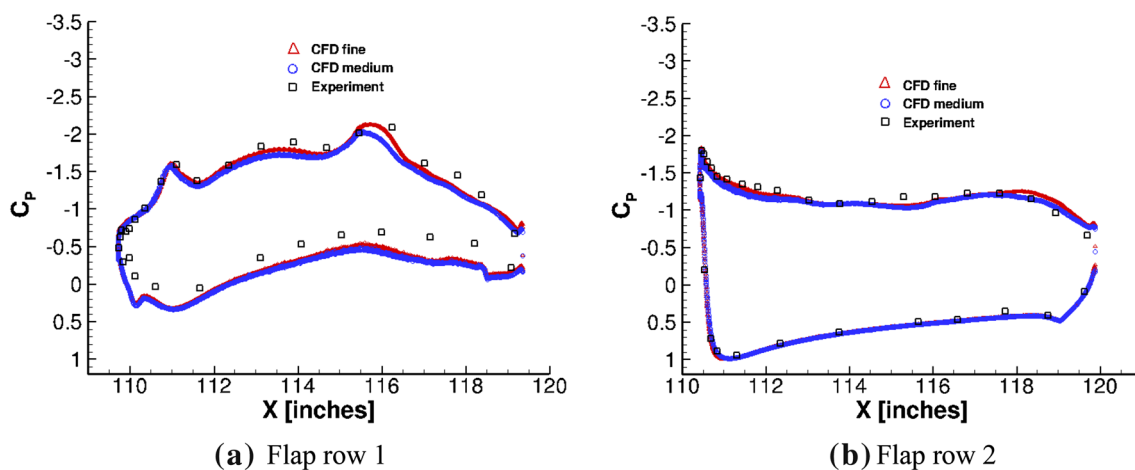
Fig. 12 Surface pressures at flap inboard edge for configuration without main gear (from Ref. [21])
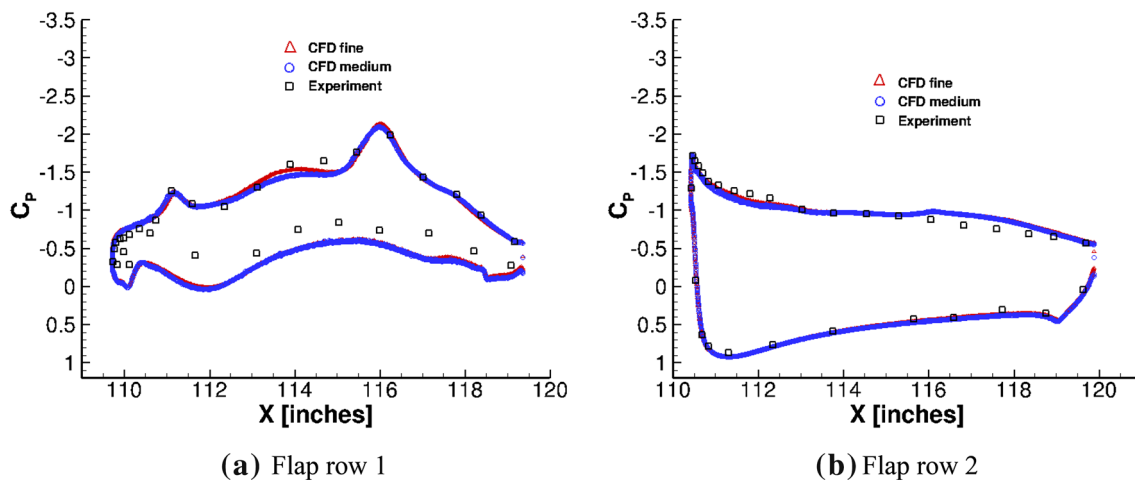

Fig. 13 Surface pressures at flap inboard edge for configuration with main gear on (from Ref. [21])

immediate vicinity of the flap inboard edge. Representative C_p distributions for the two rows closest to the inboard edge (rows 1 and 2) for a landing configuration with the main gear off and on are shown in Figs. 12 and 13. Except for a localized, slight improvement in the prediction of upper surface pressures at row 1, the two grids produced nearly identical results. Overall, good agreement with measurements was obtained. The favorable comparison displayed in Fig. 13 indicates that gear-flap interaction and its effect on the steady loading at the tip were well predicted. Our earlier comment that the gear wake is convected past the inboard portion of the flap, altering the tip loading, is confirmed by comparing the pressure coefficient plots shown in Figs. 12 and 13 for flap rows 1 and 2. Note that the row closest to the inboard flap side edge (row 1) exhibits an overall decrease in pressure difference between flap lower and upper surfaces, caused by the locally reduced inflow velocity within

the gear wake. Also, observe that the location of vortex roll-up and coalescence on the suction side of the flap is shifted downstream by about 0.05c. By the third flap row position (not shown), the differences in the surface pressure values for the configurations with and without the gear become negligible. The computed pressure distribution at the row closest to the outboard edge (row 11) is presented in Fig. 14 (the pressures measured on the flap bottom surface between $128.5 < X < 130$ inches were deemed incorrect due to bad ports after Ref. [21] was published). At this row, although the overall character of the surface pressures was captured in the predictions, the simulated time-averaged C_p values substantially underestimate the broad suction region that occurs at mid-chord; the increased spatial resolution achieved with the fine grid mildly improves the comparison for the predicted values. Nevertheless, very recent work by Mineck and Khorrami [6], who used a standard Navier–Stokes solver to
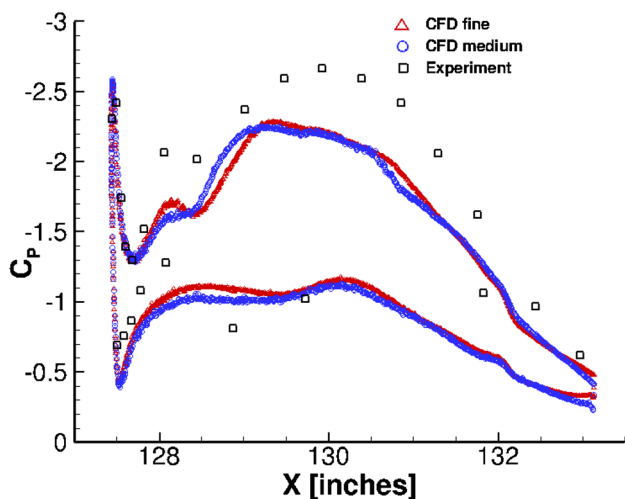
Fig. 14 Surface pressures at flap outboard edge, row 11, configuration without main gear (from Ref. [21])

study the effects of increased spatial resolution on the flap side-edge flowfield for the same model, clearly demonstrates that under prediction of the C_p values at the outboard tip is mostly related to insufficient spatial resolution.

Accurate prediction of the surface pressure fluctuations in the vicinity of the flap side edges is critical for a proper assessment of airframe noise source location. Extensive comparisons between computed and measured fluctuating pressure fields for all dynamic probe locations, presented in Ref. [21], revealed that remarkable agreement exists at most measurement positions, with some probes displaying slightly better and some others showing slightly worse, agreement than the sample power spectral density (PSD) plots that will be included here. Locations for various unsteady surface pressure probes in the vicinity of the inboard and outboard flap tips are shown in Fig. 15.
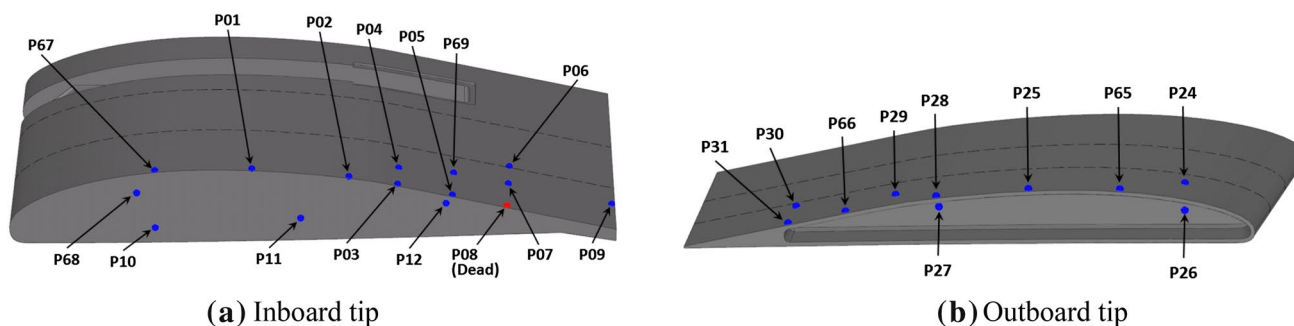

(a) Inboard tip

(b) Outboard tip

Fig. 15 Unsteady pressure transducers used on 18%-scale model flap tips (from Ref. [15])

(a) Probe 2 location, gear off

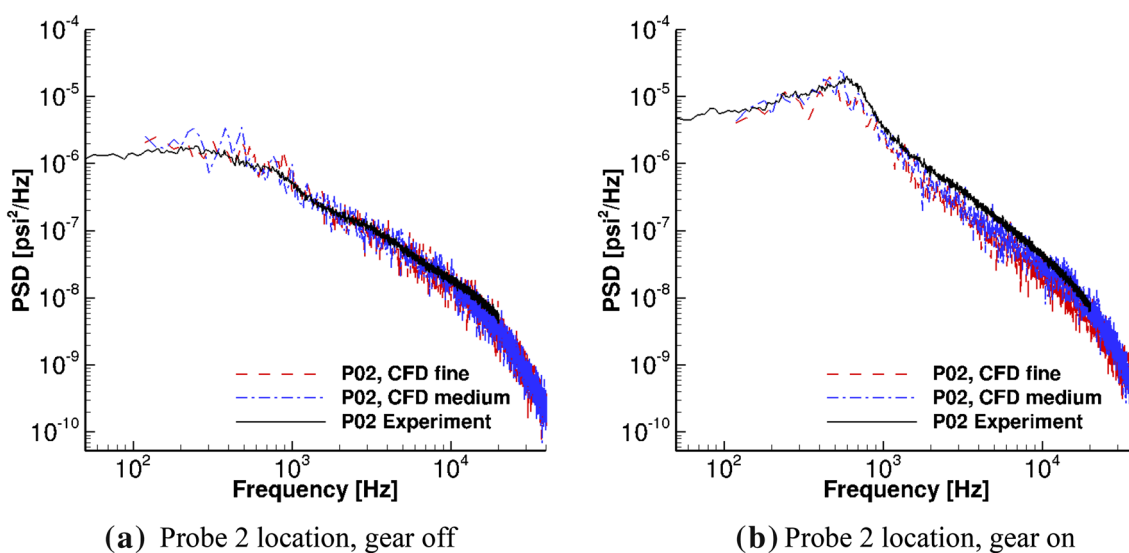(b) Probe 2 location, gear on

Fig. 16 Power spectral density of surface pressure fluctuations at flap inboard tip—upper surface edge (from Ref. [21])
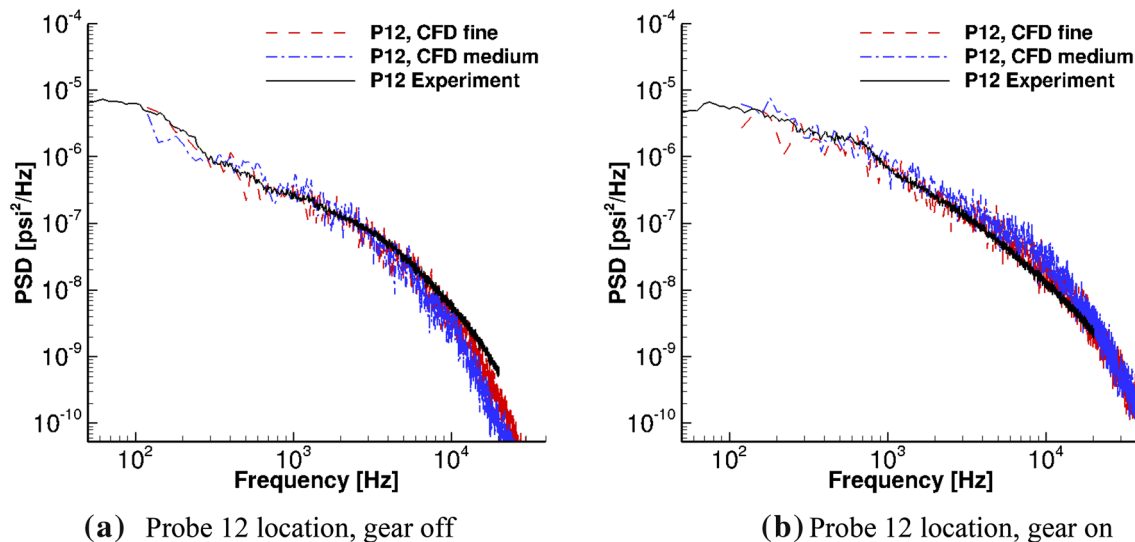
Fig. 17 Power spectral density of surface pressure fluctuations at flap inboard tip—side-edge wall (from Ref. [21])

4.1.1 Fluctuations at inboard tip

Sample simulated PSD values at a probe placed along the edge on the flap upper surface for the gear off and on configurations are presented in Fig. 16. As can be seen from the figure, medium- and fine-resolution grids produced very similar spectra at this location, with both solutions correctly predicting the measured spectrum in shape, frequency content, and energy levels. The pressure spectrum at probe 12, situated on the inboard edge-side wall, is plotted in Fig. 17 for both configurations. The good agreement obtained at this probe indicates that the sequence of fluid dynamic processes necessary for vortex inception at the edge was resolved appropriately. As shown in Figs. 16 and 17, when the main gear is on the predicted spectra are in excellent agreement with measured data on the upper surface and side-edge wall for the two grid resolutions shown. As observed from the experimental spectra, gear deployment noticeably increases the magnitude of the fluctuation levels at probes 2 and 12. The simulations capture this rise and the change in spectral shapes remarkably well, lending credence to the fact that accurate prediction of complex installation effects such as gear-flap interaction is possible.

4.1.2 Fluctuations at outboard tip

Prediction of the surface pressure fluctuations at the outboard tip was complicated by the difficulty in producing a simulated cavity that closely adhered to what was actually tested. The main differences were in the location and rigidity of the bulb seal, as well as the absence in the simulations of small ancillary elements found inside the cavity. These subtle differences made the accurate prediction of surface

pressure fluctuations at discrete locations near the outboard tip problematic at best.

Taken from Ref. [21], sample pressure fluctuations from two representative probes, one inside the tip cavity (probe 27) and one along the edge on the flap upper surface (probe 66), are presented in Fig. 18. Despite the aforementioned geometry differences, very good agreement between computed and measured spectra was attained at the outboard edge. Unlike those at the inboard tip, the spectra associated with the outboard edge contain several mild, broad tonal features that result from vortex–cavity interaction. These features were captured reasonably well even at the medium-resolution level. In general, as reported in Ref. [21], increased spatial resolution improves the predicted results.

Overall, the pressure spectra predicted with PowerFLOW® at both inboard and outboard flap tips are in remarkably good agreement with the measured PSDs for the baseline configurations without and with MLG. Since surface pressure fluctuations are essential to any noise prediction methodology, the close agreement obtained with these simulations bodes well for accurate farfield noise computations.

4.1.3 Main landing gear

Details of the measured and simulated MLG fluctuating surface pressure fields, including transducer location and numbering, are given in Ref. [21]. Sample PSD plots for a wheel probe and a door probe are presented in Fig. 19a, b, respectively. Very good agreement is observed for the former, with the predicted spectra closely tracking the measured data over most of the frequency range. Close agreement was also observed at other probe locations on both wheels (see Ref.
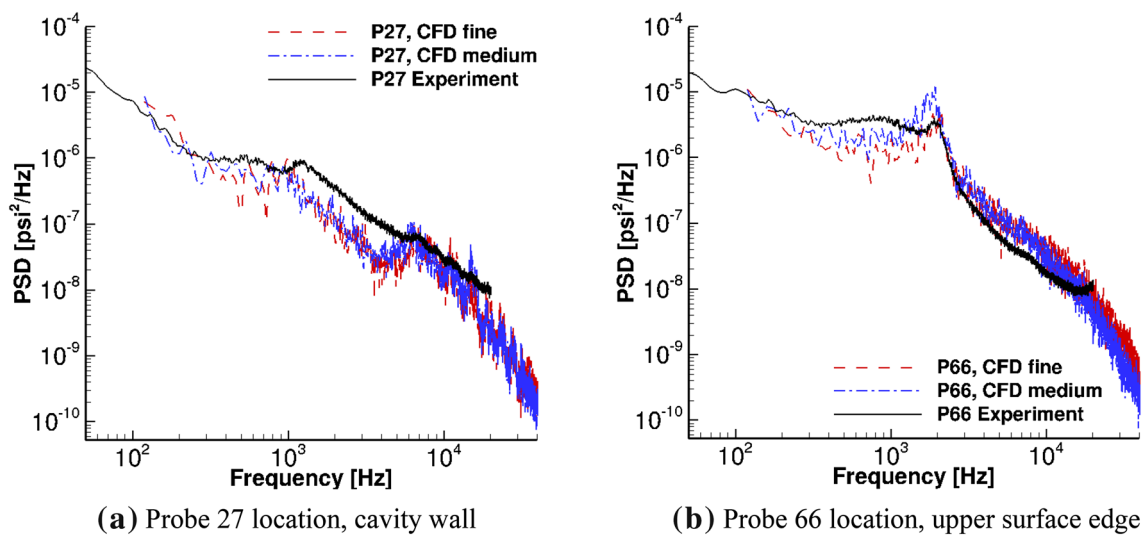
(a) Probe 27 location, cavity wall

(b) Probe 66 location, upper surface edge

Fig. 18 Power spectral density of surface pressure fluctuations at flap outboard tip with main gear on (from Ref. [21])

(a) Wheel (probe 43)
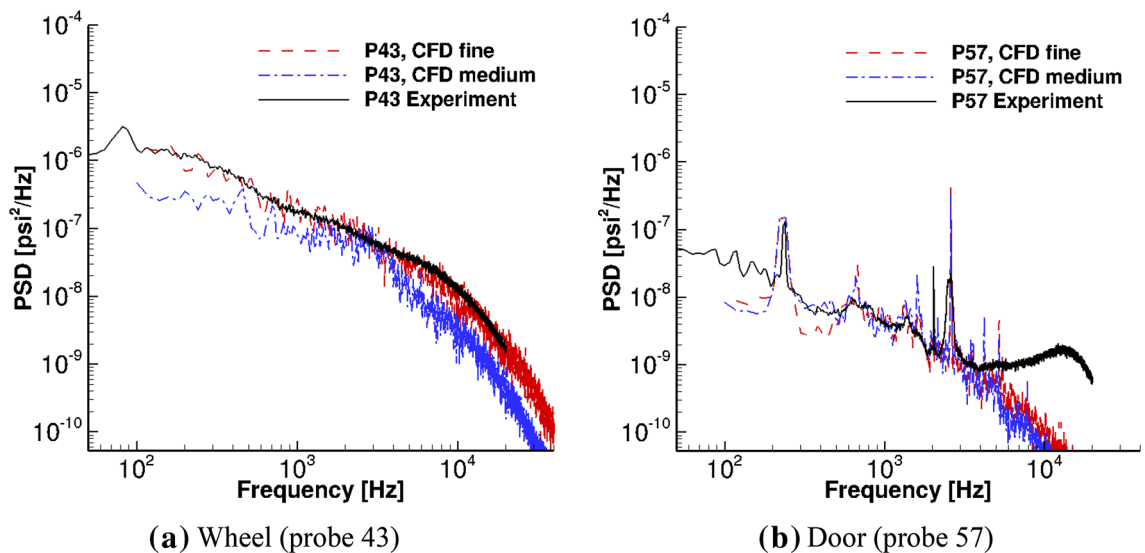
(b) Door (probe 57)

Fig. 19 Power spectral density of surface pressure fluctuations on main landing gear (from Ref. [21])

[21]). In general, increased spatial resolution improved the agreement. Sample surface pressure fluctuation spectra on the gear door (Fig. 19b) also demonstrate good agreement with measured data. Note that the pressure levels on the door are significantly lower than those on the wheel or other gear components. The simulated PSD curves capture the frequency content and the fluctuation levels up to frequencies approaching 7 kHz. At present, the underlying source of the rise in measured spectra beyond 5–6 kHz is unknown. The increased levels could be caused by hydrodynamic pressure fluctuations associated with the detached flow over the door surface or by the self-noise associated with the pinhole installation of the dynamic sensors. Nevertheless, for this aircraft configuration, the gear door does not appear to be a major noise source and most likely acts as a reflector for the acoustic waves emanating from the flap inboard tip and/or the other components of the gear. As such, note the presence of several major and minor tones on the door spectra. These tones were generated elsewhere and what was measured on the door is the resultant radiated pressure field impinging on the surface. The simulations captured most of the tonal features in the measured spectra.

Because of the bluff body nature of the various gear subcomponents, prediction of the measured surface pressure spectra at discrete locations is challenging on several fronts. For example, a slightest flow angularity in the

tunnel freestream velocity, and/or differences between the free-field computational setup and the open-jet wind-tunnel tests, can cause a significant shift in the location of flow separation and reattachment points. Even a small movement of these points may have a profound effect on the spectral shape and content at the limited number of discrete points where surface transducers were installed. A parameter better suited to judge the success of the simulations is how well the farfield acoustic behavior is predicted.

4.2 Off-surface quantities

Extensive particle image velocimetry (PIV) measurements of the 18%-scale semispan model, with a focus on mapping the flow field in the landing gear wake and within the gear-flap interaction region, were conducted in the 14×22 tunnel. The PIV apparatus and test campaign were documented in Ref. [18]. The collected data were used as a benchmark to evaluate the capabilities of the selected computational methodology. Comparison with simulated results was discussed in Ref. [35]. Representative samples are provided in this section.

The mean and fluctuating streamwise velocity (U and u', respectively) contours capturing the wake of the main gear are plotted in Fig. 20a, b. Very good agreement between the medium- and fine-resolution CFD results was attained. Most of the main flow features observed in the PIV contours were closely mapped by the simulations, even at medium resolution. Grid dependency effects are clear in the sample velocity
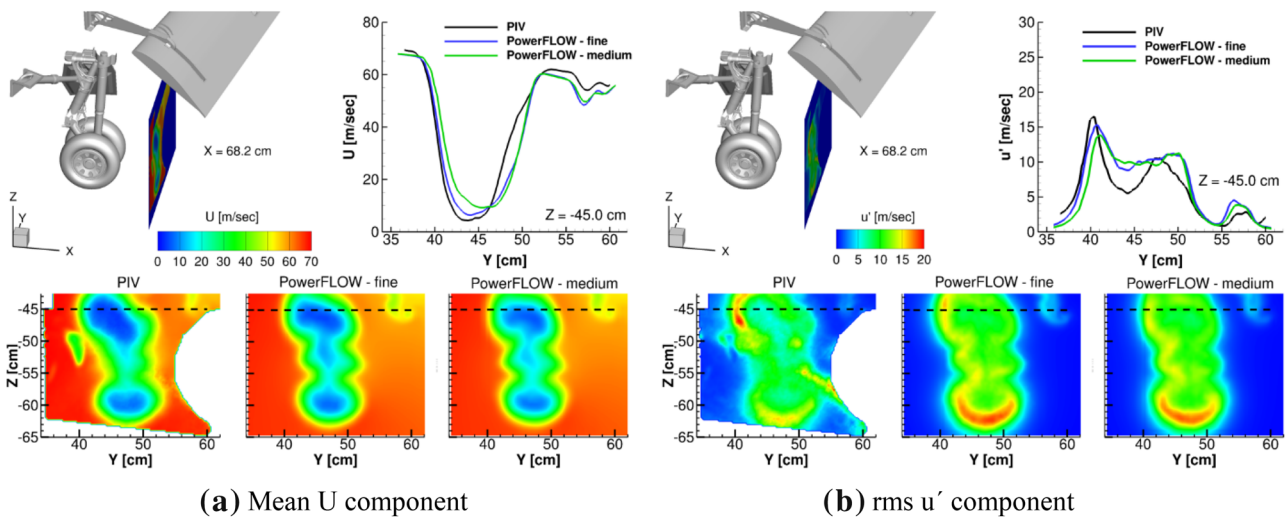

(a) Mean U component   (b) rms u´ component

Fig. 20 Spatial resolution effects on simulated flow field in gear wake (from Ref. [35])

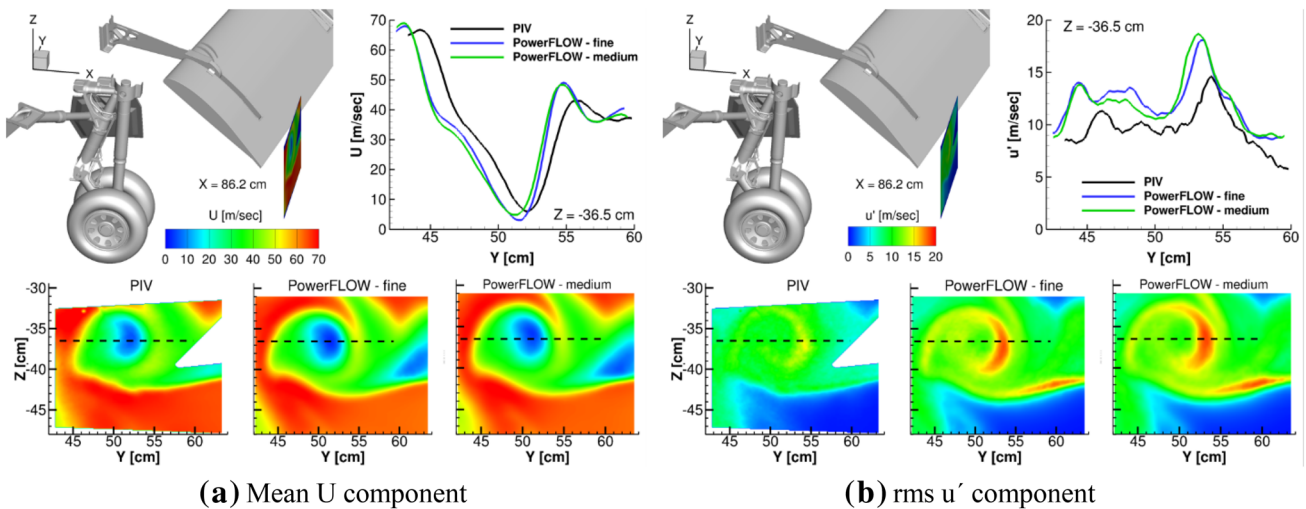(a) Mean U component   (b) rms u´ component

Fig. 21 Spatial resolution effects on simulated flow field in flap wake with main gear on (from Ref. [35])

profiles extracted along the *Y* coordinate (highlighted by the broken line in the velocity contours). Note that these effects are minor, indicating that the simulated velocities were well converged, with the finer resolution profiles being in better agreement with the PIV profiles.

A byproduct of gear-flap interaction is its effect on tip vortex evolution at the flap inboard edge. Contours of the mean and fluctuating components of streamwise velocity downstream of the flap trailing edge, for the gear deployed configuration, are displayed in Fig. 21. The simulated contours for *U* (Fig. 21a) show a grid-converged field that is in very good agreement with the measurements. Notice that the core of the tip vortex has a large velocity deficit, exhibiting wake-like behavior. The magnitude of this deficit is clearly shown in the extracted mean velocity profiles along the *Y* coordinate. Again, the CFD profiles are in reasonable agreement with each other. Note from the mean velocity profiles that there is an apparent *Y*-shift of about two centimeters in the computed vortex position relative to the measured position. This shift can be attributed to several factors, foremost among them the differences between computational (free-air) and experimental (open-jet) setups, the presence of a slight flow angularity in the tunnel incoming flow, and model deformation (aeroelastic) effects. Simulated results for *u'* are shown in Fig. 21b. The same shift in vortex position noticed in the *U* profiles is also observed here. The medium- and fine-resolution contours indicate that a fairly well converged field was achieved, while comparison with measured data reveals that the computed field contains larger amplitude fluctuations. As is the case with many other measurement techniques, larger differences are to be expected in the higher moment velocities.

The velocity field sampled at the same streamwise location as that of Fig. 21 for the configuration with the main gear removed is shown in Fig. 22. Notice from the PIV contour in Fig. 22a that, without the gear, the tip vortex exhibits a large axial velocity excess in its core. In contrast to the results shown in Fig. 21a, comparison of the medium- and fine-resolution solutions of the mean velocity contours (Fig. 22a) clearly indicates that a reasonable grid-independent state has not been attained. The plotted velocity profiles reinforce the visual inspection and capture the rise in vortex core velocity associated with increasing grid resolution. Nevertheless, as shown in Fig. 22b, a relatively good comparison with measured fluctuating streamwise velocity field was achieved.

4.3 Farfield noise signature

The ultimate and most relevant element of the validation process for the current airframe noise simulation methodology was the prediction of farfield noise. The procedure for obtaining farfield noise from the computed near-field solution and detailed comparison between simulated and measured noise spectra were documented in Refs. [21, 22]. In this section, limited results taken from these references are highlighted.

Comparisons between computed and measured farfield noise spectra obtained at the overhead location of 17.5 ft. (5.33 m) from the model as installed in the 14×22 tunnel are presented in Fig. 23. For the baseline configuration with main gear off (Fig. 23a), the broadband component of farfield noise is predicted rather well for most of the frequency range of interest. The broad tonal hump observed between 7 and 10 kHz in the measured PSD is associated with tip vortex–cavity interaction at the flap outboard side edge [16]. Vortex–cavity interaction was not captured by
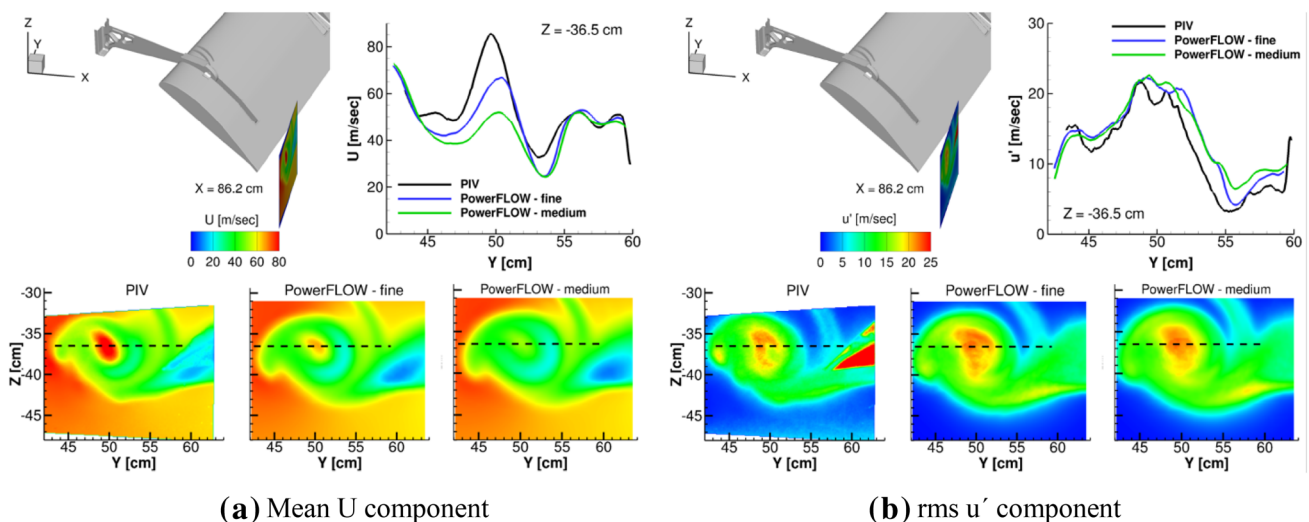

(a) Mean U component   **(b)** rms u′ component

Fig. 22 Spatial resolution effects on simulated flow field in flap wake with main gear off (from Ref. [35])
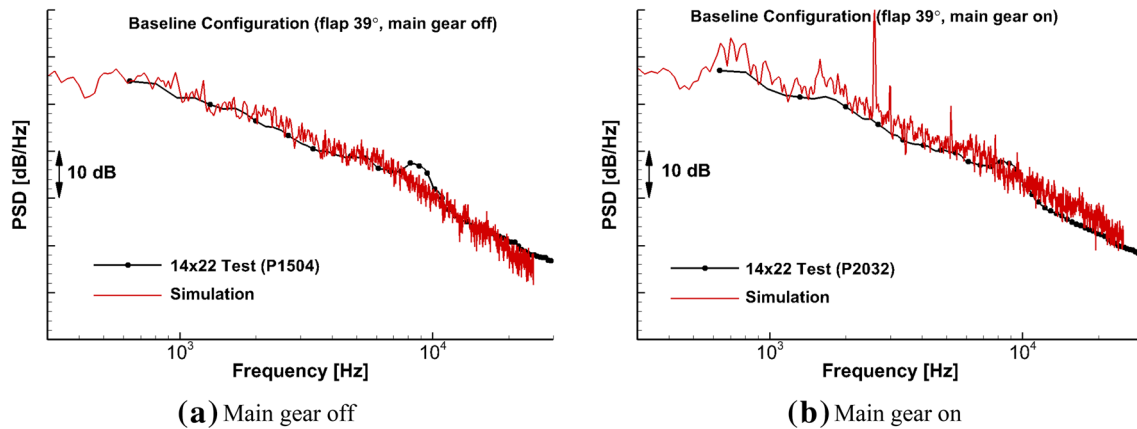
Fig. 23 Comparison between simulated and measured farfield noise spectra (from Ref. [22])

these earlier simulations because of insufficient spatial resolution. Close agreement was also attained for the configuration with main gear on (Fig. 22b). The very prominent tone centered around 2.5 kHz in the simulated spectrum is produced by the main gear hollowed front post with the cavity opening being exposed at the knee joint [22]. During the acoustic test of the model, after the initial set of runs, this tone was eliminated by taping the cavity face at the joint.

4.4 Mach and Reynolds number effects

The resounding success of the validation study conducted for the 18%-scale model provided ample confidence in the ability of the selected computational approach to determine two other important trends, namely M and Re effects. Additional simulations of the configuration with flap deflected 39° and MLG removed were conducted at $M = 0.16$ and $M = 0.24$, representing ±20% deviation from the baseline speed. For these simulations, the fluid viscosity was kept constant to represent a true change in airspeed. While present in the computed solutions, the corresponding 20% variation in Re was deemed insignificant and did not alter M effects in any noticeable fashion. All other numerical parameters and mesh were kept the same.

As shown in representative plots contained in Fig. 24, changes in M influenced the time-averaged pressure coefficients slightly, producing a small compressibility effect on the order of 1% for the model lift coefficient, C_L, which is consistent with the value derived using a simple Prandtl–Glauert M transformation.

Sample PSD plots for surface probes located at the flap inboard and outboard tips are displayed in Fig. 25. Note that the local fluctuating surface pressures show an obvious variation with M. Scaling of the PSD levels according to M^4, in conjunction with a linear frequency shift based on Strouhal number (St) scaling, produces an excellent collapse of the
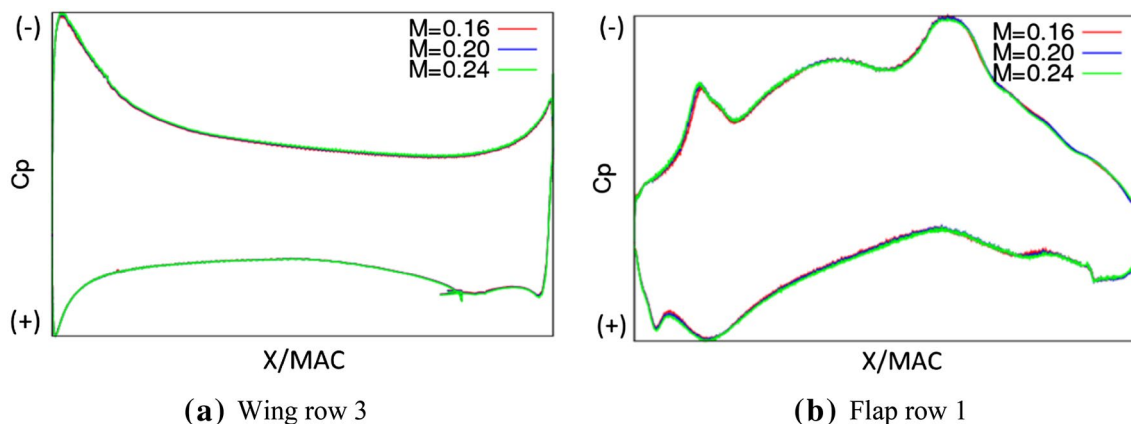

Fig. 24 Surface pressures at wing inboard and flap inboard edge for baseline semispan configuration without main gear

(a) Probe 10, inboard flap tip

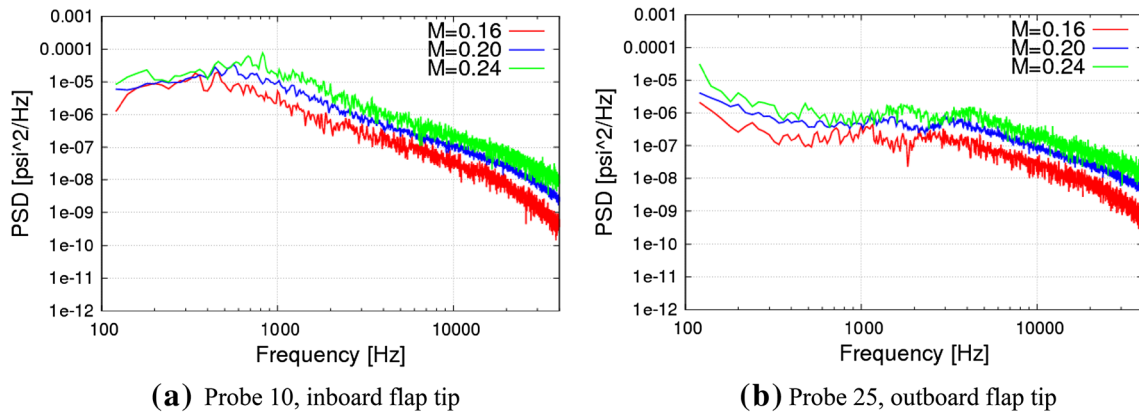**(b)** Probe 25, outboard flap tip

Fig. 25 Unscaled power spectral density of surface pressure fluctuations at flap inboard and outboard tips, baseline semispan model without main gear
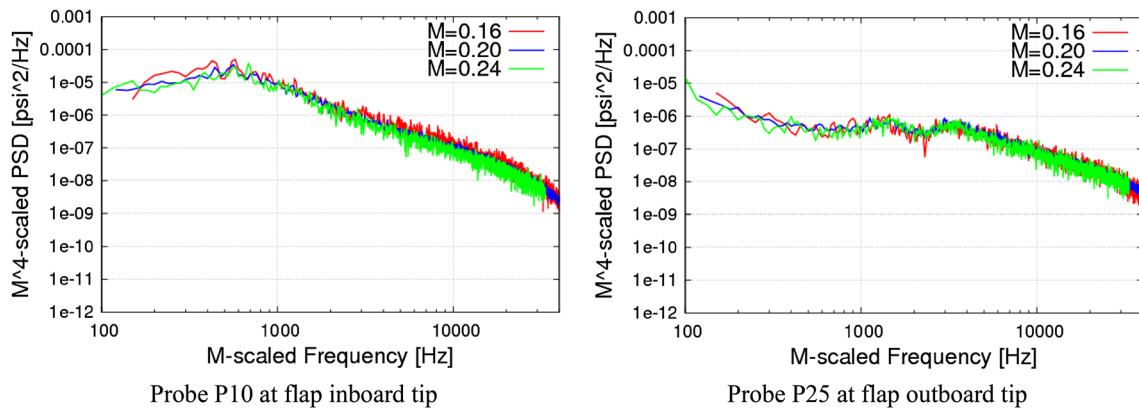

Probe P10 at flap inboard tip

Probe P25 at flap outboard tip

Fig. 26 M^4 scaled power spectral density of surface pressure fluctuations at flap inboard and outboard tips, baseline semispan model without main gear

(a) No Scaling

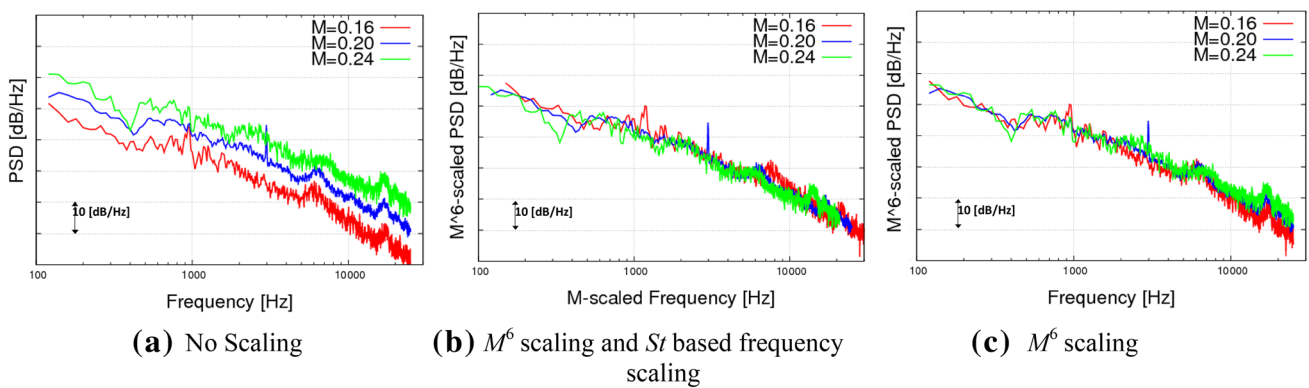**(b)** M^6 scaling and St based frequency scaling

(c) M^6 scaling

Fig. 27 Power spectral density at the farfield location, baseline semispan model without main gear

spectra (Fig. 26) signifying that the pressure field is dominated by the hydrodynamic component.

Corresponding simulated farfield noise spectra are presented in Fig. 27. As seen in Fig. 27b, application of

typical $\sim M^6$ scaling in conjunction with St based scaling of the frequencies fail to produce a crisp collapse of the computed spectra (except maybe for frequencies above 10 kHz). A better collapse of the spectra is obtained without

frequency scaling (Fig. 27c), thus corroborating similar trends reported in Ref. [20] for the 18%-scale model acoustic measurements. Nevertheless, both surface and farfield spectra scaling confirm that the dominant noise sources for this configuration are of dipole-type, which justifies the use of a FWH approach based on solid walls to obtain farfield acoustic behavior.

The model configuration with a flap deflected 39° and MLG deployed was chosen to examine Re effects. An important objective of this exercise was to isolate the effects of Re from those of geometry prior to extending the computational methodology to the full-scale, complete aircraft. The viscosity and temperature of the freestream air are independent input variables within PowerFLOW®. Thus, Re and M can be adjusted separately. For this study, Re was increased from 3.4×10^6 to 10.5×10^6 while keeping M constant at 0.2. The latter Re value, which represents 50% of flight Re for this aircraft, was sufficient to capture the most relevant trends at a substantially reduced computational cost, as will be shown later.

Grid density was adapted globally to enable use of the same resolution for the boundary and shear layers at the increased Re while maintaining the same mesh refinement strategy. This process nearly doubled the number of volume and surface elements required for the simulation.

Solutions obtained at both Re produced very similar flow patterns at each of the four flap brackets and formation of flap tip vortices. Only minute differences in vortex roll-up and the resulting pressure imprint on the surface at the outboard flap tip region were observed.

For the 18%-scale model, global aerodynamic lift increased by ~3% for the higher Re. The difference in model drag between the two solutions was less than 0.3%, with the higher Re producing the lower value. The discrepancies in lift are relatively small and spread over most of the model wing and flap, as shown in the sample plots of Fig. 28. Only pressure row 11 at the flap outboard tip (Fig. 28d) shows a noticeable Re dependency. This effect is manifested in the formation of a stronger vortex on the flap upper surface near the leading edge, followed by increased suction in the broad pressure peak (caused by the primary tip vortex) that starts in the mid-chord region and extends to the trailing edge.

A snapshot of the vortex formation region near the inboard flap tip (Fig. 29a, b) shows a high degree of similarity in the larger flow structures between the two Re solutions and a rather qualitative agreement in the resolved smaller structures for the higher Re case, as seen in Fig. 29b. These finer flow features are attributable to the physical and numerical resolution of turbulent flow structures at smaller length scales that are present due to increased Re.

Sample PSD plots of the fluctuating surface pressures at select sensor locations in the vicinity of the flap inboard (probes P01 and P06) and outboard (probes P24 and P25)

tips are shown in Fig. 30. Observe that, at most probe locations, the spectral shape, frequency content, and magnitude of the fluctuating pressure field were found to be comparable for the two model-scale simulations. Nevertheless, at some sensor locations (e.g., probes P24 and P25, Fig. 30c, d, respectively) differences emerge. In particular, the presence of new peaks in PSD near the outboard side-edge (Fig. 30c) is mostly driven by the tip cavity that houses a bulb seal (see Fig. 4), as documented in Ref. [15].

Sample PSD plots for the fluctuating pressure field on the main gear are displayed in Fig. 31. Spectral data at measurement probe locations on the gear door and rear strut are presented. The probe situated on the lower part of the door (Fig. 31a) shows very similar spectra for the two semispan, 18%-scale model simulations. Large differences are observed for the probe located near the blunt leading edge and the connecting rod of the door (Fig. 31b). These variations are associated with slightly different local flow separation due to Re effects. As mentioned earlier, the pressure fluctuations on the door are much smaller than those at the flap tips or other components of the MLG, that is, the main gear door is not a prominent noise source for this aircraft and mostly acts as a reflector for impinging acoustic waves generated at other locations. Therefore, the differences in unsteady surface pressure observed at discrete locations have minimal impact on the farfield noise. In contrast, some of the highest pressure fluctuations on the gear are produced at the rear strut near the impingement point for the detached shear layer emanating from the front post. As such, the rear strut is a major contributor to farfield noise. The PSD curves from the two model-scale simulations for the probe located on the rear strut (Fig. 31c) are very similar in shape and levels up to the mid-frequency range of 2 kHz. As expected, for frequencies above this range, the model-scale simulation performed at Re of 10.5×10^6 yields higher spectral levels due resolution of finer scale turbulent flow structures.

Farfield sound pressure level (SPL) directivity maps for the 18%-scale, semispan configuration at the two simulated Re are displayed in Fig. 32. Both maps show a similar distribution in terms of directivity pattern and magnitude of the noise being radiated to the ground. However, the higher Re solution (Fig. 32b) predicts slightly higher noise levels in the mid-frequency range in the forward direction.

The farfield spectra at an overhead location 5.33 m (17.5 ft) away from the model, which corresponds to the position of the microphone array during the 14×22 test, are presented in Fig. 33. The spectra for both semispan simulations are very similar, including the tonal hump associated with the landing gear cavity that occurs at about 200 Hz. Also note from the figure that other peaks in the mid-frequency range generated by the gear and flap outboard tip cavities are also present in both simulations, but are typically more pronounced for the higher Re case. As anticipated, with increased Re, elevated
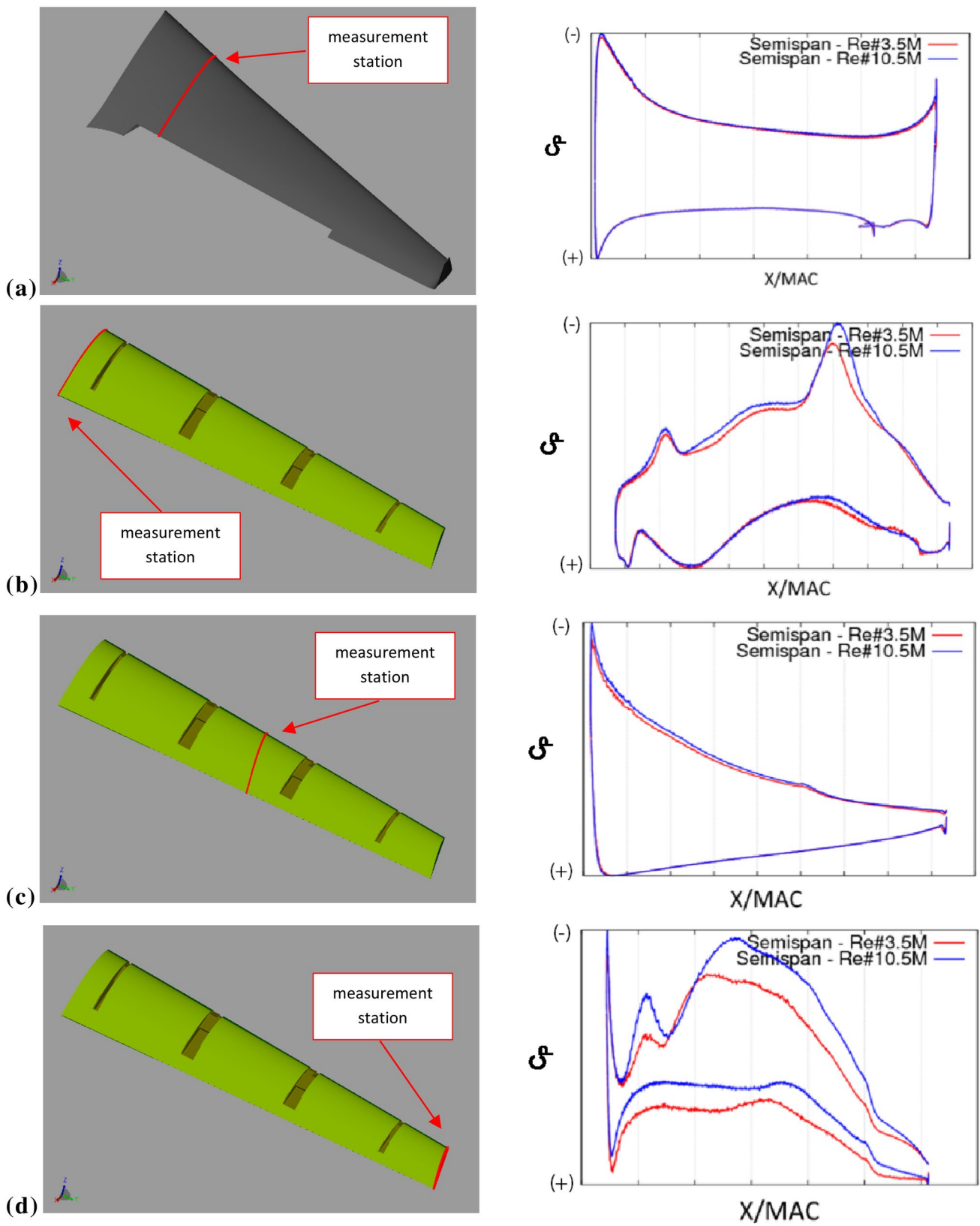
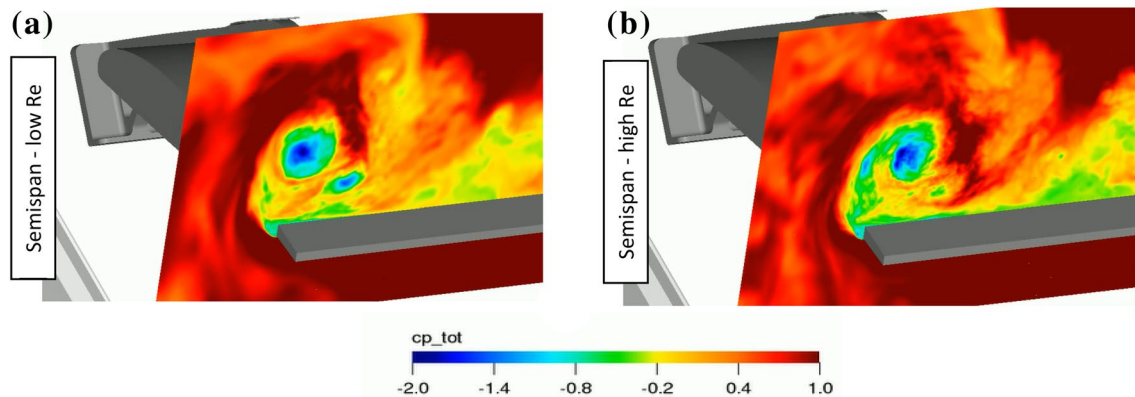**Fig. 28** Pressure distribution at various sections on the wing flap (from Ref. [23])

Fig. 29 Instantaneous flow structures at the inboard flap (from Ref. [23])

broadband noise levels at high frequencies are present. The spectral comparison for the two simulations (Fig. 33) confirms that the lower *Re* sufficiently reproduces the appropriate trends and conditions for airframe noise investigations at *Re* encountered during flight test.

5 Full-scale simulation results

The high physical fidelity of the 18%-scale model geometry and the accuracy and quality of the corresponding computed results made extension of the LBM-based simulation methodology to the full-scale, complete aircraft configuration a natural step. We now focus on the full-scale simulations and some of the associated issues that made the task uniquely complex. The computations presented here were executed at $M = 0.2$. $Re = 10.5 \times 10^6$, roughly half the flight *Re* (based on the full-scale wing mean aerodynamic chord and aircraft landing speed), was chosen for the simulations. This value was selected after the modest study targeting *Re* effects, presented in the previous section, was completed. Said study revealed that, at $Re = 10 \times 10^6$, scale effects on steady and unsteady surface pressure fields diminished significantly. Accordingly, we believe that the farfield noise levels obtained at this *Re* are nearly equivalent (at a lower computational cost) to the corresponding levels at the full flight *Re*.

As a first step, solution convergence was examined carefully. Given the resource-intensive nature of the present computations, the study was used to determine the most efficient VR setup and the minimum required spatial resolution that would yield a relatively grid-converged solution within a reasonable computational cost. Relying on the experience gained from the 18%-scale model predictions [21], simulations on coarse-, medium-, and fine-resolution grids were performed. The global VR setup and mesh refinement strategy developed for the subscale computations was adopted to

enable similar resolutions for the boundary and shear layers at the increased *Re* of 10.5×10^6. A summary of the computational attributes and resources for the largest case (flap 39° and main gear deployed) is presented in Table 2.

Sample results of steady and unsteady surface pressures from the baseline configuration of flaps deflected 39° with MLG on (deployed), which represents the most computationally demanding configuration, are presented next to highlight some of the more pertinent trends. The locations of the steady pressure rows and unsteady pressure probes, and the naming convention used to identify them, are the same as those used for the 18%-scale model study [14, 15].

5.1 Solution dependency on mesh resolution

Time-averaged pressure distributions on the aircraft wing and flaps are shown in Fig. 34 for the coarse, medium, and fine grids, whose results are shown in black, blue, and red symbols, respectively. Note that well converged wing and flap loading was obtained even at the medium-resolution level. The only significant spatial resolution effects occur near the flap tip regions, as observed in Fig. 34c, d. At the inboard edge, the time-averaged pressure field is well converged and only minor differences between the solutions obtained from the medium and fine grids are observed. At the outboard edge (Fig. 34d), however, while the overall pressure distribution trends are maintained, the magnitude of the pressure coefficient on the flap suction side shows noticeable differences with grid resolution. Solution convergence is not monotonic, since the coarsest results lie between the medium- and fine-resolution solutions. We attribute this behavior to the highly complex, non-linear interaction that occurs between roll-up of the free shear layer and the flow field associated with the tip cavity housing the bulb seal. This interaction causes jitter in the spanwise position of the tip vortex resulting from the rolled up shear layer,
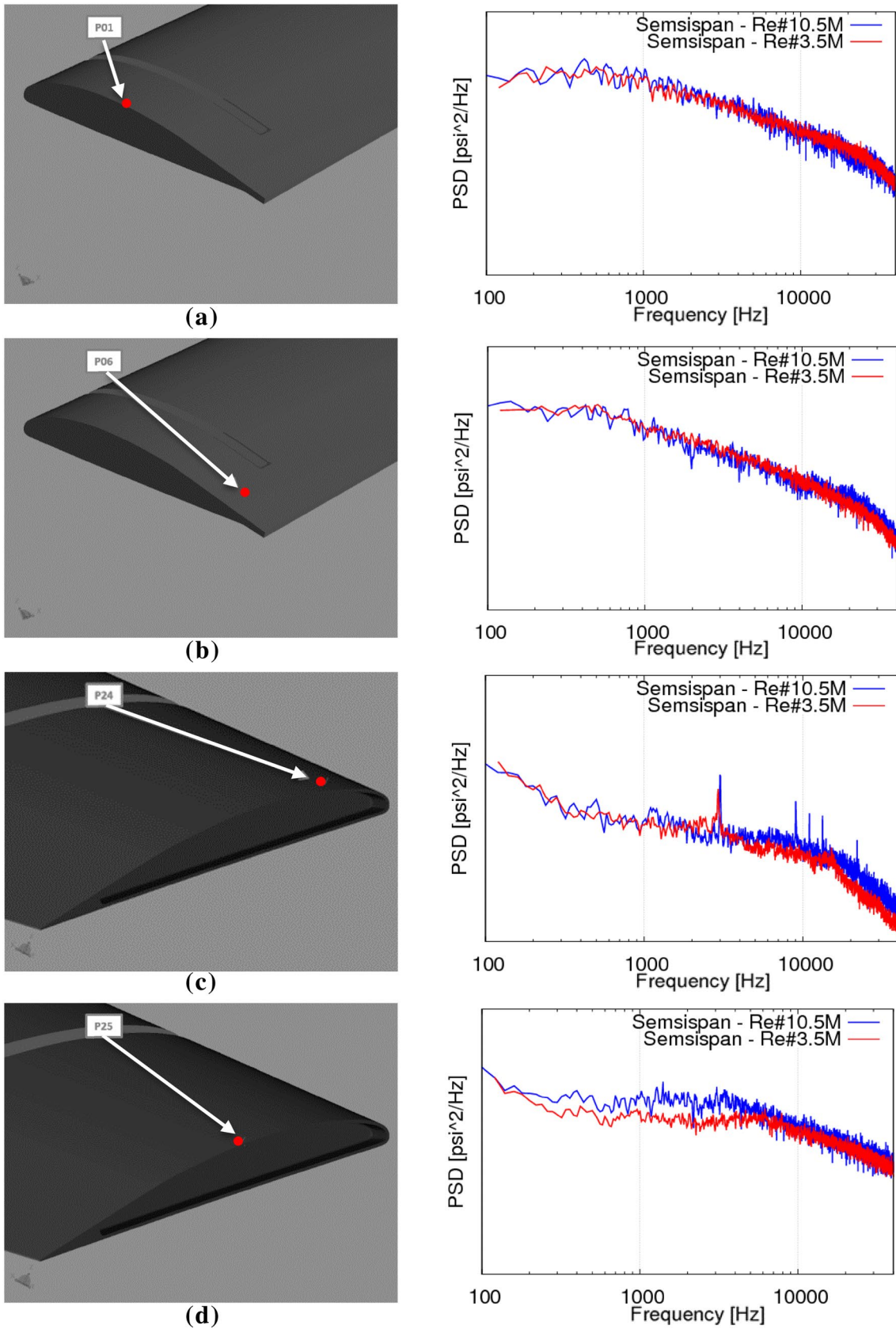
Fig. 30 Pressure spectra of surface probes on the flap side edges (from Ref. [23]). Frequencies are model-scale
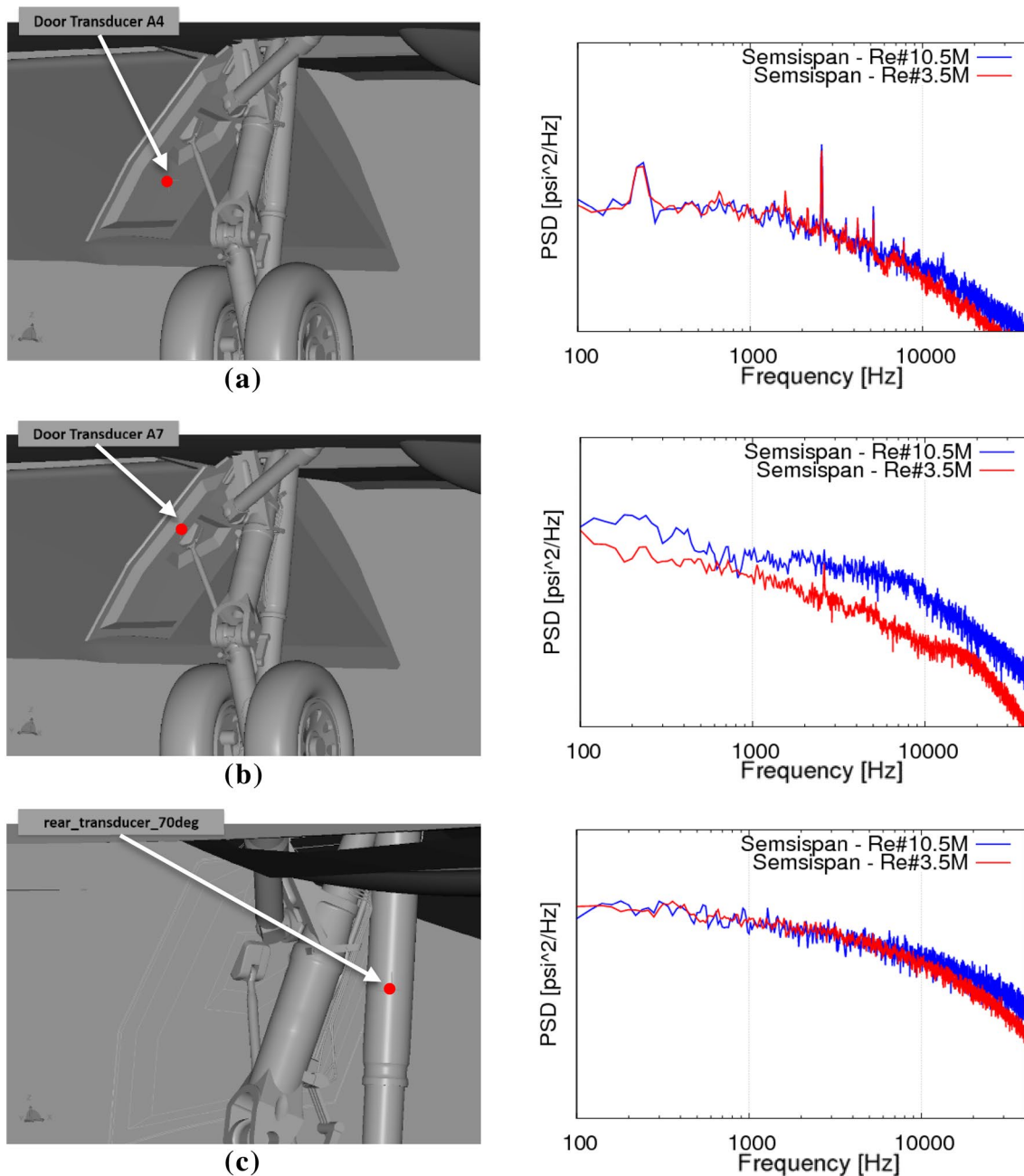
Fig. 31 Pressure spectra of surface probes on MLG geometry (from Ref. [23]). Frequencies are model-scale

thus making the time-averaged spanwise vortex location extremely sensitive to grid refinement.

An equally important aspect of solution quality is convergence of the surface pressure fluctuations. As representative sample results, we have picked two probe locations at each flap tip to discuss resolution effects on the time-dependent pressure field. PSD spectra for the two probes located at the inboard tip, one positioned near the edge (probe 3) and one away from the edge (probe 6), are plotted in Fig. 35a as functions of full-scale frequency. A nearly grid-independent

solution was achieved. We remark here that solution convergence at other probe locations on the inboard tip was similar, with some probes showing slightly better and some probes slightly worse results than those depicted in Fig. 35a. PSD results for the two representative probes at the outboard tip are displayed in Fig. 35b. The surface pressure spectra collected at probe 27, which is located inside the tip cavity, show a good collapse of the data obtained from the three grids indicating that the cavity flow field is properly captured even at the medium-resolution level. In contrast, the spectra
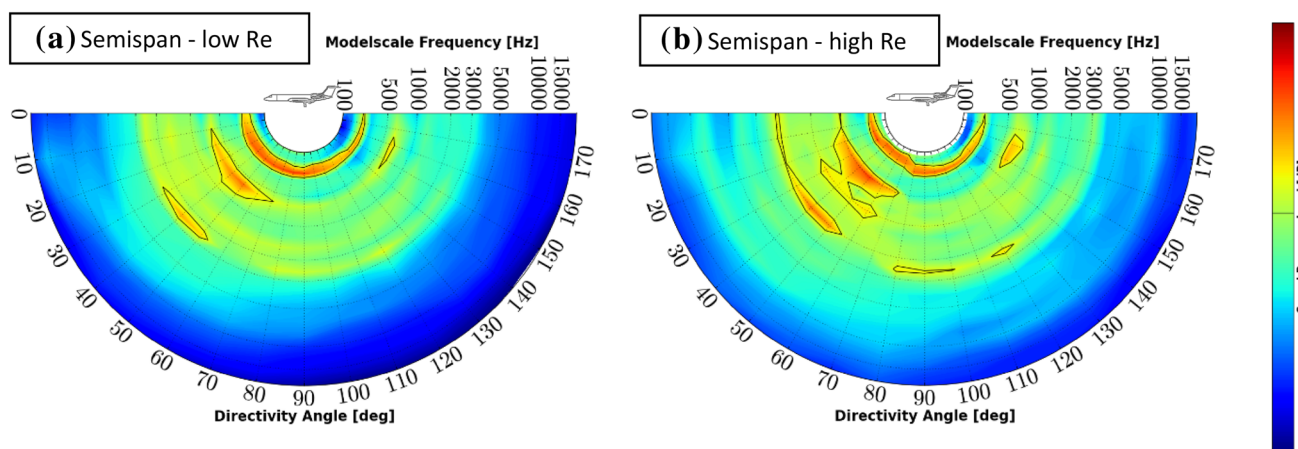
Fig. 32 Farfield SPL directivity maps reproduced from Ref. [23] (0° indicates aircraft forward flight direction)
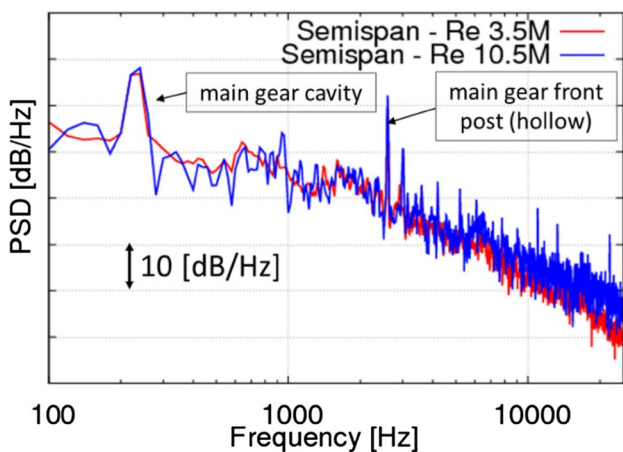

Fig. 33 Farfield pressure spectra (overhead position) for the semispan simulations (from Ref. [23]). Frequencies are model-scale

the lower frequency content of the spectra displays a gradual movement toward a mesh independent solution. As noted earlier, we believe that such behavior is caused primarily by low frequency variations in vortex position relative to the side edge as the grid resolution is increased. A small span-wise movement of the tip vortex could potentially instigate disproportionately large variations in the local fluctuating surface pressures at the same location, very much like those displayed for probe 30. In general, solution dependency on spatial resolution at most probe locations examined is rather small, with behavior consistent with that shown for probe 27 (Fig. 35b). Thus, noticeable differences in PSD levels at a few discrete points should not be used to judge solution accuracy.

5.2 Validation of surface pressures

The only fully vetted, published aerodynamic measurements of a Gulfstream aircraft are those obtained during the 18%-scale, semispan model tests in the LaRC 14×22 tunnel [14, 15, 17]. Although we expect some differences due to *Re* and geometry effects [23] in regions where

at probe 30, positioned away from the edge under the path of the primary tip vortex, indicate a significant variation with mesh resolution. As observed for the time-averaged pressure distribution at the outboard tip (Fig. 34b), the convergence behavior of the PSD levels is not monotonic. In fact, even

Table 2 Simulation statistics

Baseline Full span—full scale	Coarse resolution	Medium resolution	Fine resolution
Minimum cell size (mm)	0.745	0.497	0.331
Volume elements (10^6)	896	2609	8396
Surface elements (10^6)	62	108	287
Simulated time (s)	3.0	3.0	3.0
Time steps	2,453,077	3,679,615	5,519,422
Cores used for computation	2000 Ivy	4020 Westmere	12,000 Ivy
Surface sampling frequency (Hz)	25,551	38,327	57,490
CPUh (10^3)	190	991	~7000

(a) Wing

(b) Midspan flap

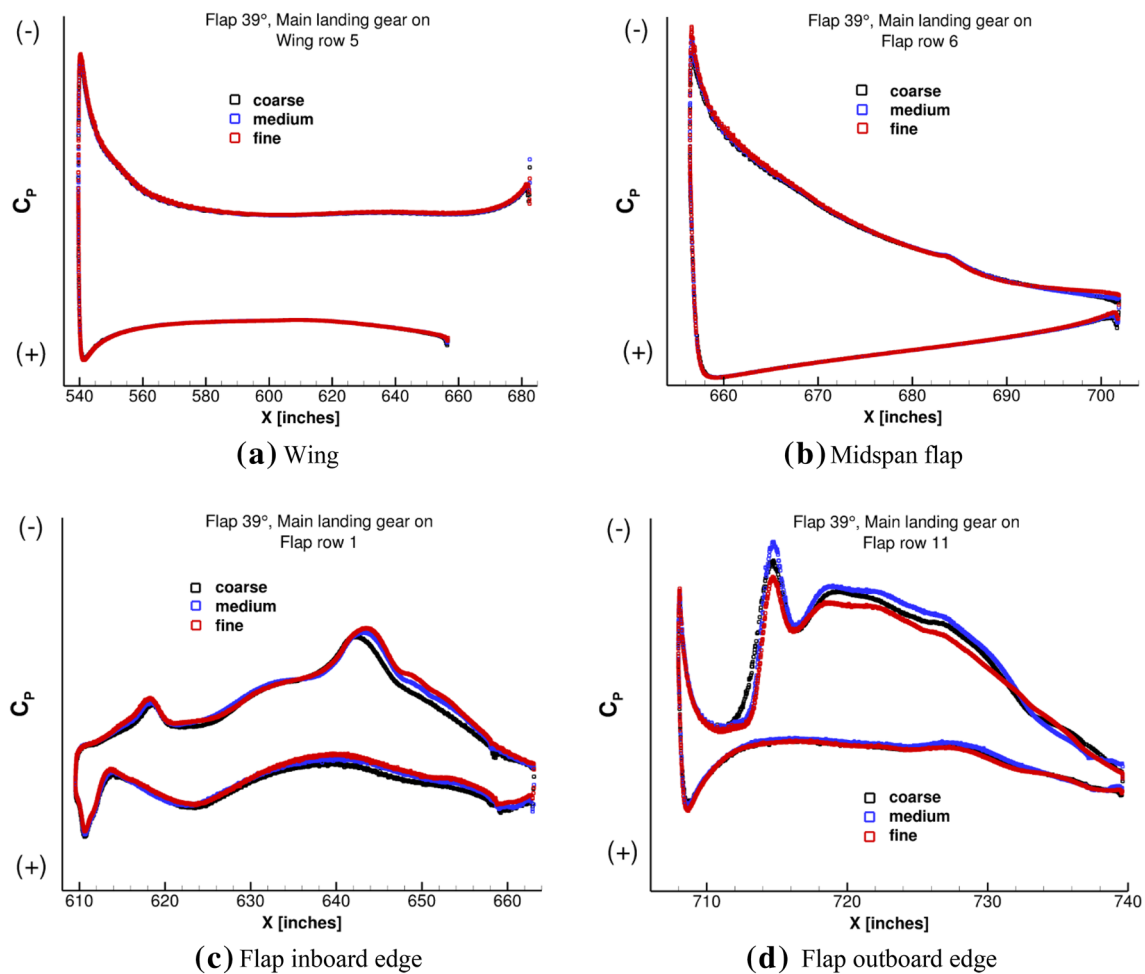(c) Flap inboard edge

(d) Flap outboard edge

Fig. 34 Time-averaged pressure distributions on aircraft flap (from Ref. [30])

significant flow unsteadiness exists (i.e., flap tips, main gear, etc.), comparison of simulated, full-scale surface pressures with those measured for the 18%-scale model provides valuable insights on the accuracy of the present simulations. For completeness, the previously obtained and validated model-scale computational results [21] have also been included in the comparative plots that follow. In these plots, the model-scale data have been converted to full-scale values using appropriate scaling factors.

Sample plots comparing computed full-scale, time-averaged pressures with measured model-scale values are presented in Fig. 36. As shown in the figure, the pressure distribution on the wing remains nearly constant except for a minor increase in suction at the leading edge and toward the trailing edge. Since the full-scale wing is an enlarged replica of the model-scale wing, the small changes observed are purely caused by Re effects. The pressures on the flap also indicate that a close correspondence exists between full- and model-scale data, especially at the

mid-span and inboard tip rows. The most noticeable differences occur at row 11, which is situated adjacent to the flap outboard edge (for this row, pressure measurements on the flap bottom surface between $128.5 < X < 130$ inches were deemed incorrect due to bad ports after Ref. [21] was published). At this location, the observed increase in pressure differential between the upper and lower surfaces is mostly due to the added geometrical complexities of the full-scale tip cavity and bulb-seal assembly, and to a lesser extent to Re effects [23]. Despite the differences, the overall character of the outboard tip loading generally follows the trends observed for the 18%-scale model.

Sample comparison plots for the fluctuating surface pressures are given in Fig. 37. For consistency, PSD results are provided at the same probe locations as those used to discuss solution convergence. Model-scale PSD levels and frequencies have been converted to full-scale values using appropriate frequency scaling factors to maintain the same Strouhal number (St). At the flap inboard tip (probes 3 and

(a) Inboard tip
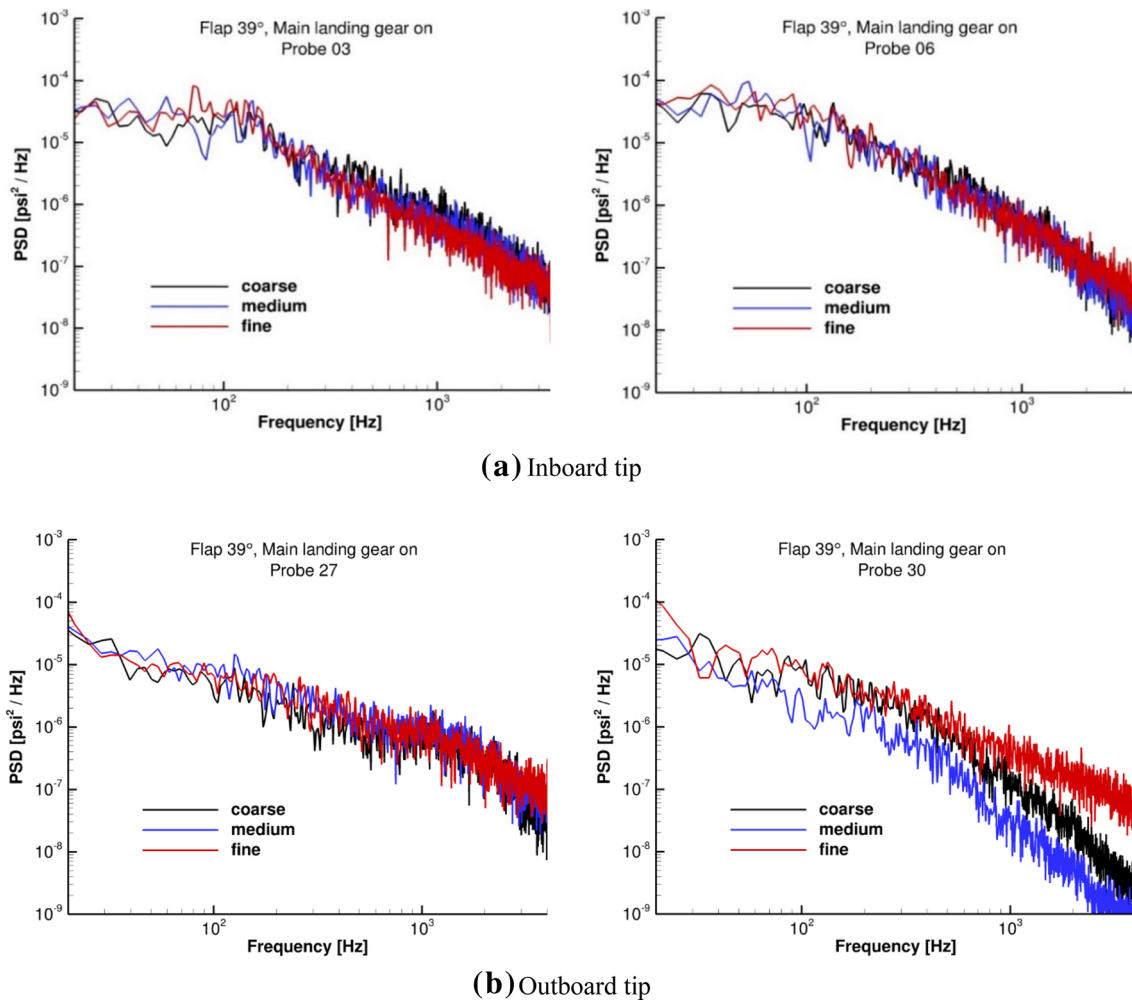

(b) Outboard tip

Fig. 35 Fluctuating surface pressure field at select locations near flap tips (from Ref. [30])

6, Fig. 37a), the extracted full-scale spectra are in close agreement with both measured and simulated model-scale data. In general, for most probes located near the inboard tip, good agreement between the computed full-scale spectra and model-scale measurements was observed. Unsteady pressure spectra at the outboard tip are shown in Fig. 37b. As anticipated, noticeable differences between full-scale, simulated spectra and wind-tunnel measurements are present. We note that similar differences also exist between measured and simulated model-scale results. As was the case for the time-averaged pressure distribution in the outboard tip region, inherent *Re* and geometry effects associated with the full-scale spectra are the main causes of the observed differences. However, the overall character and trend of the simulated fluctuating pressure field at the outboard tip are in agreement with those observed for the 18%-scale model, highlighting the enhanced physical fidelity of this model and the near-relevant flow environment produced by it.

Although not presented here, comparison of the unsteady pressure field measured on the MLG showed trends similar to those observed at the flap outboard tip. That is, while good correspondence between full-scale and model-scale spectra was observed at most probe locations, considerable differences emerged at some positions. This behavior was expected, since the full-scale main gear contains finer geometrical details that were absent in the 18%-scale model that was tested and simulated. In addition, *Re* effects also play an important role in altering the highly non-linear flow field associated with the multitude of bluff bodies that constitute such a complex gear.

5.3 Farfield noise spectra

A farfield noise spectrum computed from the full-scale simulation, along with model-scale results, obtained at the two *Re* values for the landing configuration with flaps deflected 39° and main gear deployed are presented in Fig. 38. The
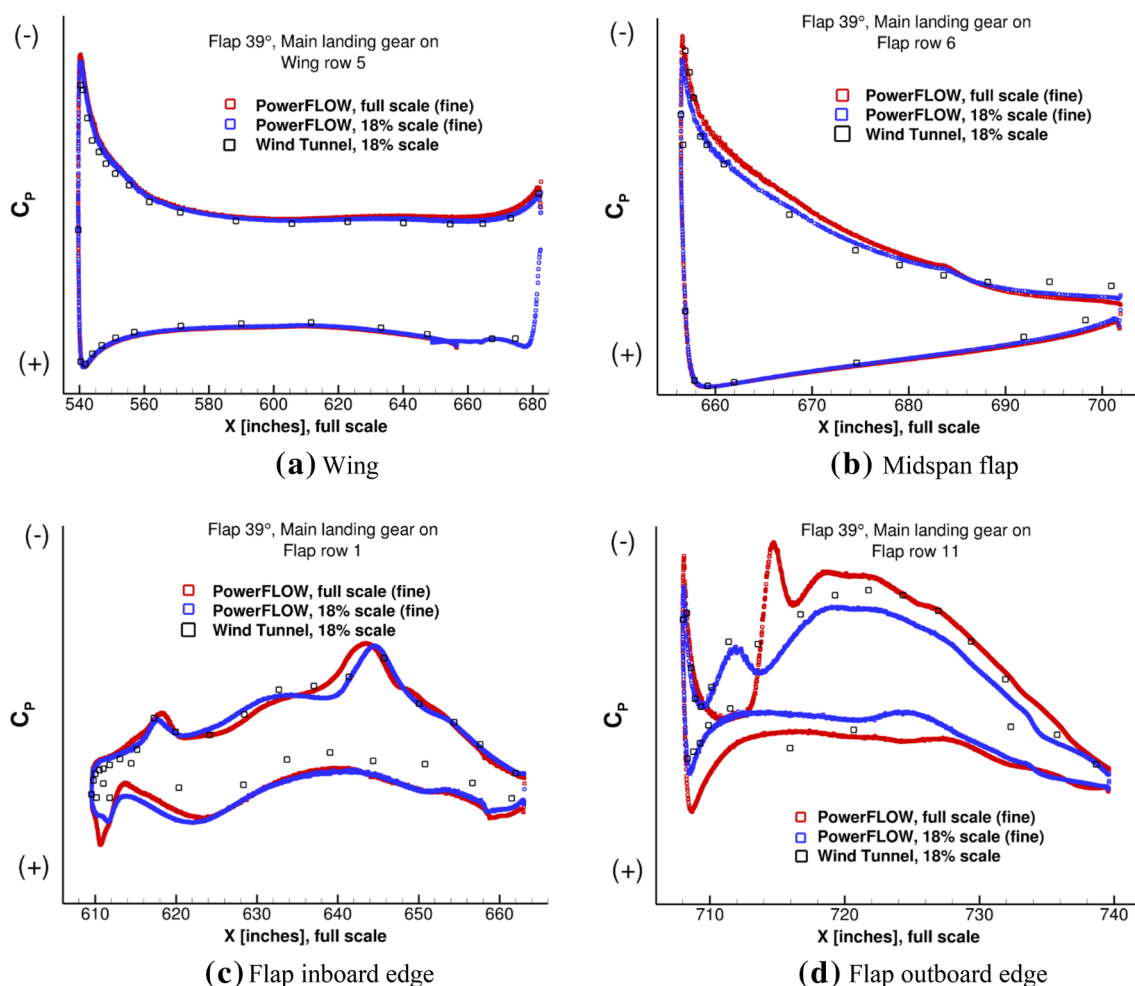
Fig. 36 Time-averaged pressure distributions on aircraft wing and flap (from Ref. [30])

wind-tunnel overhead microphone distance has been scaled for comparison purposes. Additionally, only the contribution from the starboard half of the full-scale geometry has been recorded and the model-scale spectra have been scaled for consistency. The relative position of the farfield microphone for model- and full-scale configurations is the same; the frequencies and PSD levels were scaled to maintain a constant *St*. Inspection of the plots in Fig. 38 reveals that spectral shape and level, including the low frequency tonal hump associated with the gear cavity at ~ 40 Hz, closely follow the semispan model trends up to the full-scale frequency of ~ 1000 Hz. Starting around 1.5 kHz, the full-scale spectrum shows elevated noise levels at higher frequencies. This increase is attributed mostly to self-induced noise from the more complex full-scale flap brackets and clearly exemplifies the critical role finer geometrical details play on the farfield noise signature. This important issue is discussed further in the following sections.

5.4 Global view

A global picture of the simulated vorticity field for the landing configuration of flaps deflected 39° and main gear deployed is presented in Fig. 39. As mentioned earlier, this configuration is the most complex and computationally intensive of the simulated cases considered as baselines. The figure clearly depicts where the most prominent flow unsteadiness occurs. As expected, the flap inboard and outboard tips, as well as the MLG, produce high-amplitude flow fluctuations. Also prominent in this figure is the level of flow unsteadiness that is generated by the flap brackets.

The radiated sound field produced by this aircraft configuration is given in Fig. 40. The two-dimensional planar cut, positioned near the flap leading edge, clearly shows the origin of the stronger sound waves as they radiate spherically from both inboard and outboard flap tips. Close proximity of the MLG to the inboard flap tip precludes separation of the noise generated by each component. Although less noticeable than the noise originating from the flap tips, the
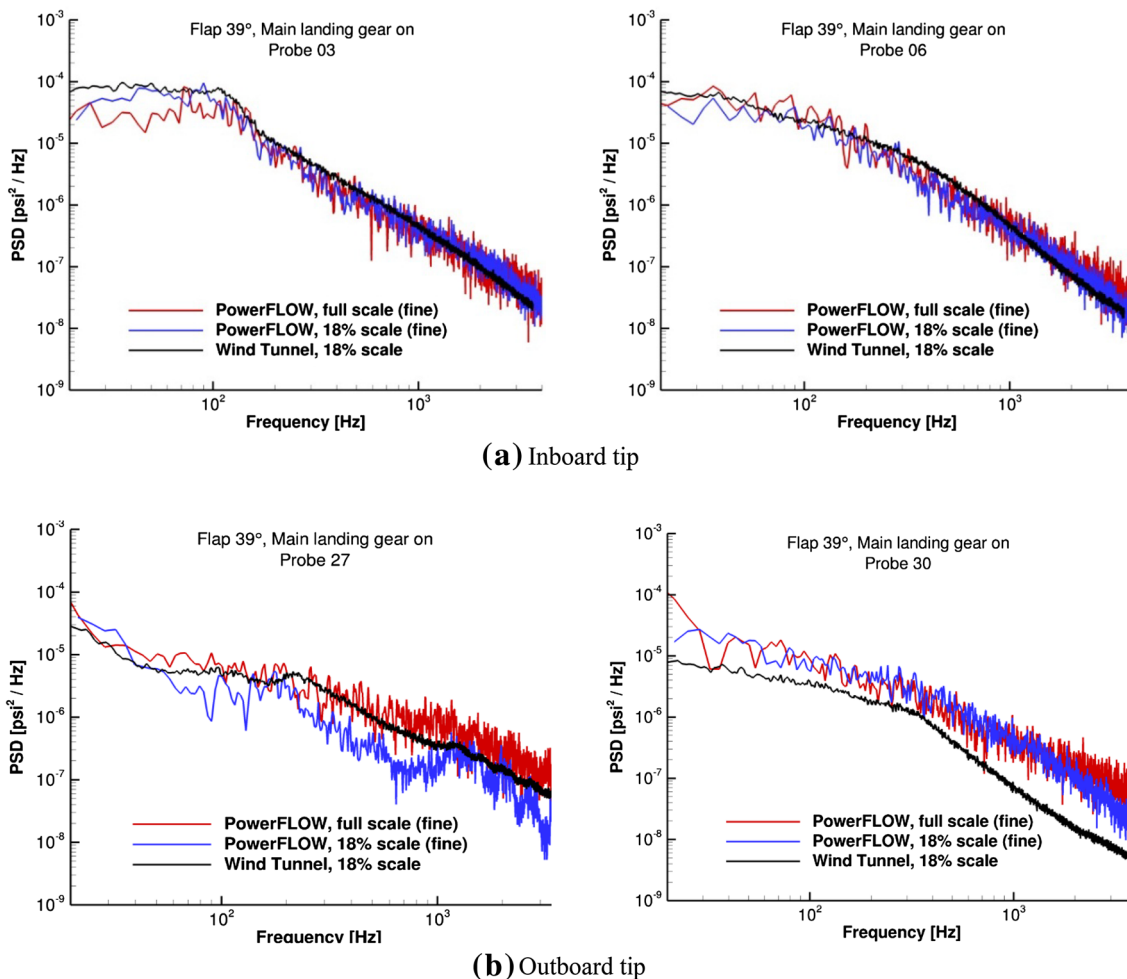
Fig. 37 Unsteady surface pressures at select locations near the flap tips (from Ref. [30])
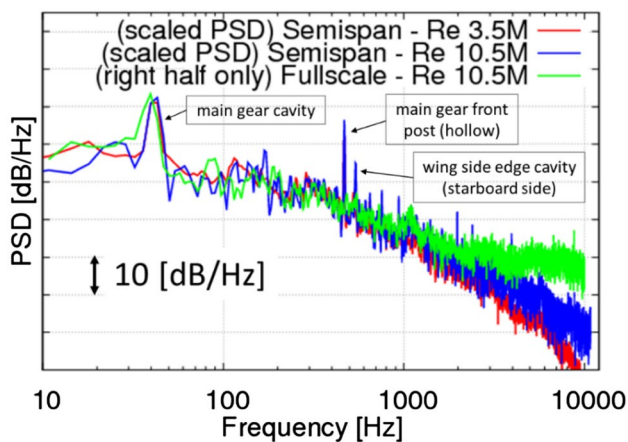

Fig. 38 Scaled farfield pressure spectra at overhead position (from Ref. [23]). Frequencies are full-scale

waves generated by the brackets are clearly discernible. As shown in Fig. 40 and discussed in the next section, the flap brackets on this aircraft are important secondary sources that contribute a significant amount of noise in the mid- to high-frequency range.

5.5 Geometric detail effects

Major geometrical variances between the full-scale, full-span model and the semispan model result from differences in configuration size (18% vs. 100% scale), consideration of additional components (vertical and horizontal tails and better representation of the main gear cavities being connected through the fuselage), and inclusion of the finer details for the full-scale configuration. The latter are mostly related to the flap bracket assemblies, the cavity and associated bulb-seal assembly at the outboard tips, and the main gear dressing. Because of the significant effect flap bracket geometry has on farfield noise, only these secondary noise sources will be discussed here.

Fig. 39 Instantaneous vorticity field based on isosurface of λ_2 criterion for 39° flap deflection and main gear deployed configuration (from Ref. [30])
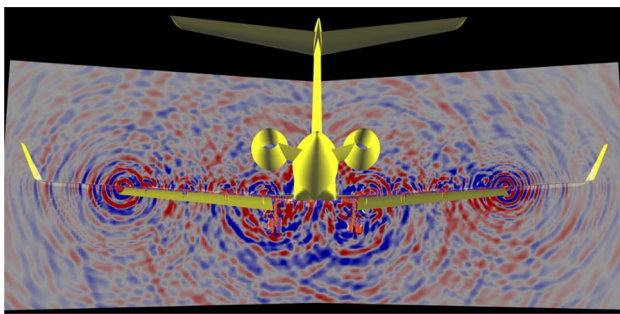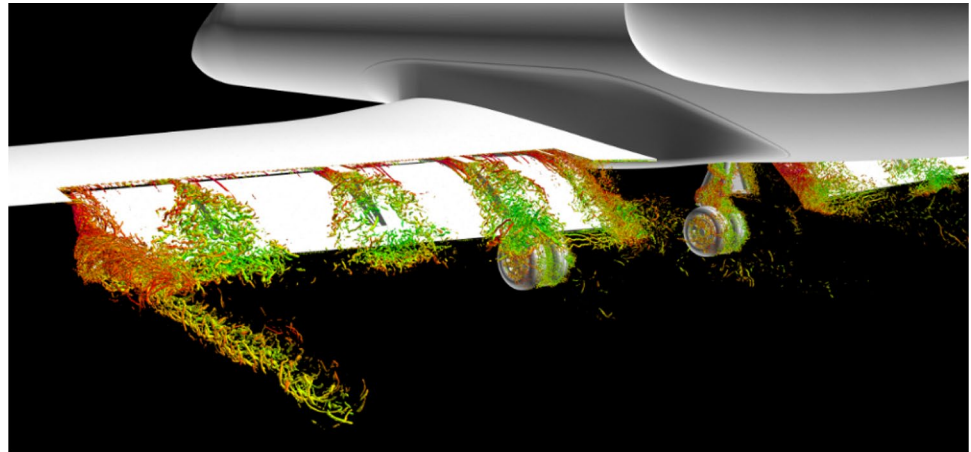

Fig. 40 Radiated sound field (dilatation field) associated with baseline configuration for 39° flap deflection and main gear deployed configuration, planar cut near flap leading edge (from Ref. [30])

5.5.1 Effect of flap bracket geometry on full-scale simulations

Testing of the 18% scale semispan model in the 14×22 tunnel revealed that the flap brackets could be important

secondary noise sources [16]. Although the model-scale brackets were carefully reproduced from full-scale design drawings provided by GAC, fabrication and instrumentation limitations necessitated geometric simplifications and inclusion of wire bundles in the vicinity of the middle two brackets. The current full-scale, full-aircraft simulations, free of such limitations, corroborated and quantified the true importance of the flap brackets and their ancillary assembly as prominent secondary noise sources contributing significantly to the farfield noise signature at medium and high frequencies. To examine the impact of bracket noise in more detail, two additional configurations were investigated on the full-scale geometry. For the first one, various relatively small gaps and holes in the bracket geometry that were not fully resolved in the original simulation have been closed. Most of these small openings were the result of missing screws, bolts, and other surface definition mismatches in the original full-scale geometry descriptions, as partially identified in Fig. 41. This configuration is referred to as "modified brackets". The second configuration is identical
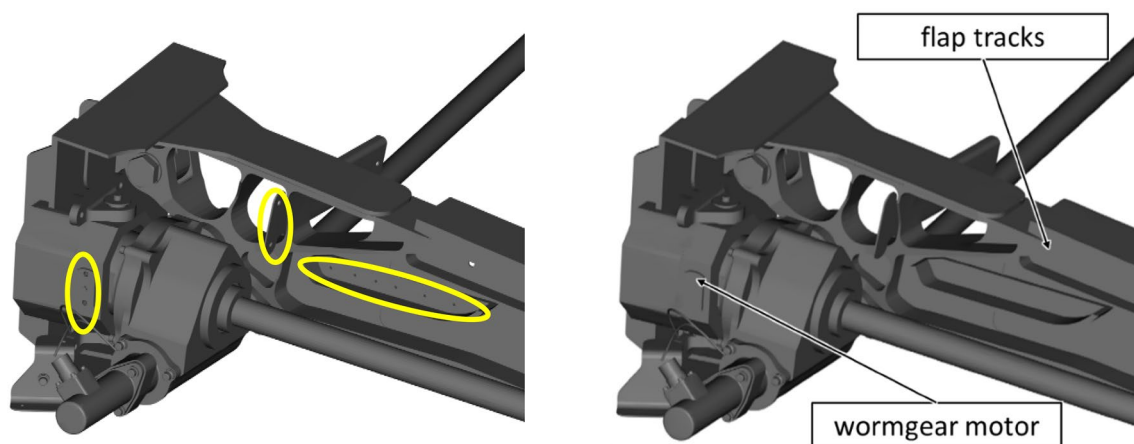

Fig. 41 Original (left) and modified (right) brackets, with various closed small holes highlighted (Ref. [23])
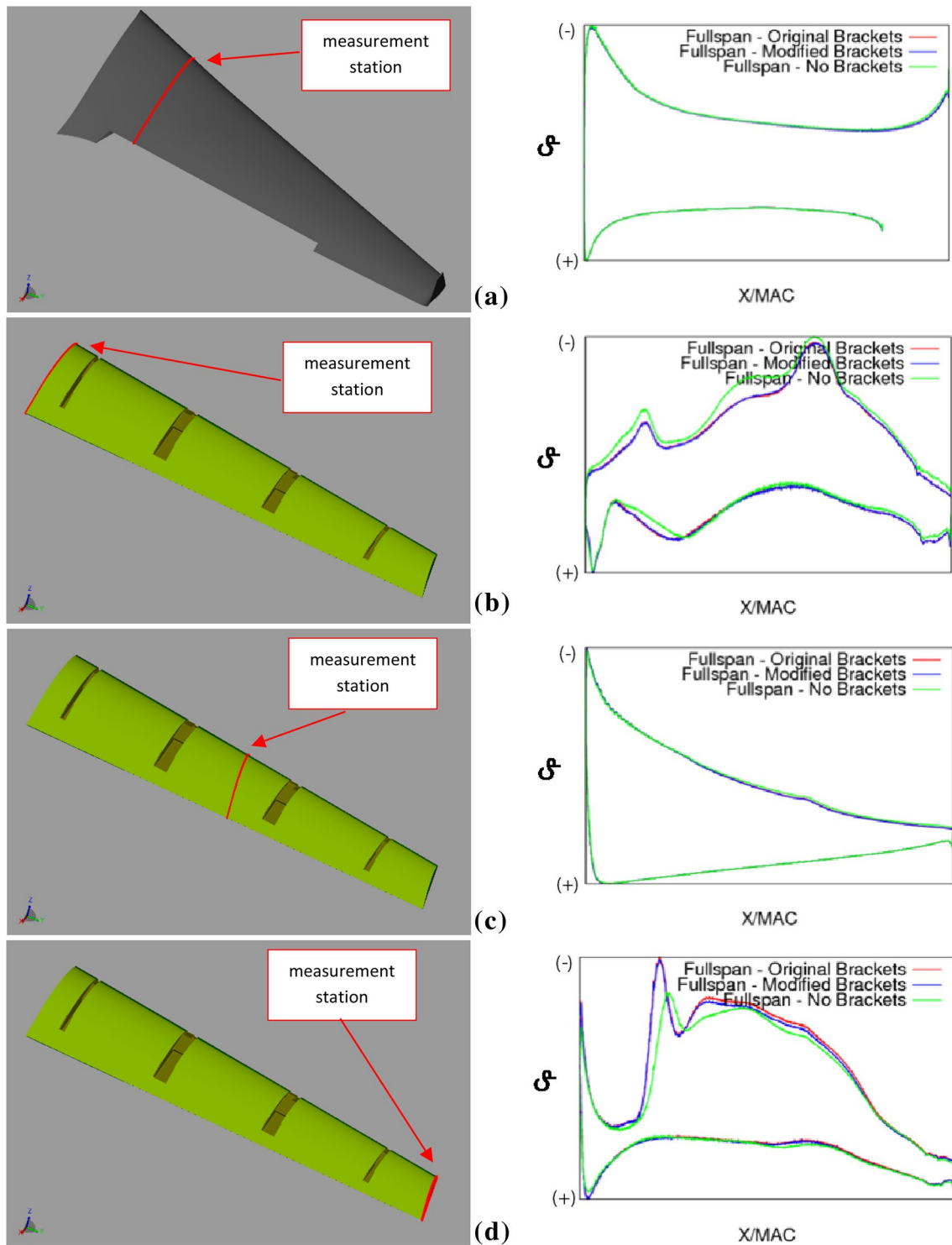
Fig. 42 Pressure distribution at various sections on full-scale wing and flap (from Ref. [23])

to the original baseline, except that all brackets, including the worm gear assembly, have been removed, i.e., the flaps are not connected to the main wing. However, the flap track retraction cavities (which house the brackets when the flap is retracted) and vanes were maintained. This configuration is referred to as "no brackets".

All three configurations produced very similar patterns of flow separation in the flap bracket regions, flap loading, and formation of flap side-edge vortices. The resulting global lift change is negligible for the modified bracket configuration, whereas an increase of 0.3% is obtained when the brackets are removed entirely.

Pressure distribution on the wing was not affected by the modifications nor removal of the flap brackets (Fig. 42a). C_p distributions on the flap at three spanwise locations are plotted in Fig. 42b–d. The midspan row (Fig. 42c) depicts a pressure distribution that is nearly the same for all bracket configurations. In contrast, removal of the brackets causes noticeable alteration of the time-averaged pressure field at the two primary noise-producing regions adjacent to the inboard (Fig. 42b) and outboard (Fig. 42d) side edges. Nevertheless, the alterations can be considered moderate, with the pressure distributions at either tip maintaining their overall character relative to the original bracket configuration.

PSD plots for probe locations within the flap tip regions are shown in Fig. 43. In general, the unsteady pressure field in the vicinity of the side edges remains unaltered for the modified bracket case, but reveals modest changes in the spectral levels (mostly at higher frequencies) at some of the surface probe locations for the no brackets case. The pressure fluctuations on the MLG were nearly the same for the three bracket configurations and, therefore, are not presented here.

Farfield spectra at an overhead microphone positioned 120.7 m away from the aircraft are shown in Fig. 44. The same position was also used to calculate overall sound pressure levels (OASPL). Note from the figure that, as expected, the reduction in spectral levels is proportional to the "cleanliness" of the bracket configuration. The decrease in levels starts modestly in the mid-frequency range and becomes increasingly larger at higher frequencies. Since high-frequency noise levels are more than 10 dB below broadband peak values (occurring at 150 Hz), the observed level of reduction may seem inconsequential. However, this is not the case as the calculation of perceived noise levels (PNL) and effective perceived noise levels (EPNL) emphasizes the high-frequency content of the spectrum. To highlight this point, we have used D-weighting (which closely tracks the weighting used for PNL computations) to demonstrate the contribution of the brackets to the farfield OASPL: the modified and no bracket configurations produce noise differences of 2.4 dBD and 2.9 dBD, respectively, as compared to the original brackets. These differences became very relevant during evaluation of several airframe noise reduction concepts on the same geometry [31] when it became apparent that bracket noise masked the full acoustic potential of the flap tip treatments being evaluated. The farfield propagation analysis reported here did not include atmospheric absorption effects.

5.6 Farfield noise signature

As described in Ref. [30], the farfield noise computation used an FWH propagation formulation [34] based on the fluctuating pressure field acting upon the solid surfaces of the complete full-scale aircraft. The data sampling frequency for this field was 57 kHz. Predicted noise spectra were calculated for a farfield microphone located 120 m (394 ft) from the aircraft center of rotation, which corresponds to the flyover certification point. For comparison with available flight-test data, the simulated spectra were corrected for atmospheric absorption using as reference a standard acoustic day of 25 °C and 70% relative humidity. The data were also corrected to facilitate direct comparisons with acoustic measurements from the 2006 flight-test campaign. A detailed account of the procedure used to compute the farfield noise spectra is provided in Ref. [30].

One-third octave SPLs computed at the 90° flyover position for the baseline case of 39° flap deflection with the main gear retracted are shown in Fig. 45. Results from medium- and fine-resolution simulations for both original and modified brackets are plotted. Very good agreement between prediction and certification microphone measurements from the 2006 flight test was attained. Note that most of the differences occur at frequencies above 2 kHz, where higher uncertainties caused by local atmospheric effects during the flight test may be present. Also present at high frequencies is residual propulsion noise, even though the engines were operated at near idle conditions during flyover. For frequencies up to 1 kHz, the simulated spectra are very similar indicating that grid resolution and bracket effects are not impacting the farfield noise signature. Above 1 kHz, bracket noise increases gradually with frequency. A drop in spectral levels with increasing grid refinement is observed at higher frequencies for the original bracket configuration. This drop is mostly associated with the elimination or reduction of high-frequency tones generated by under-resolved small openings. Also note that better resolution reduces the differences between the noise levels obtained with the original brackets and those associated with the modified brackets. In contrast, grid refinement has a very modest impact on high-frequency noise for the modified bracket configuration. The fact that some of the smaller holes covered in the simulations could remain open in an actual aircraft precludes a clear determination of bracket noise levels. In our opinion, the high-frequency component of the farfield spectra computed for the configurations with flaps deflected should lie between the original and modified bracket levels.

The configuration with flaps deflected 39° and main gear deployed is the closest to a complete aircraft in landing that was attempted with the finest resolution available; therefore, it constitutes the most computationally challenging case. Farfield SPL spectra for this configuration are shown in Fig. 46.
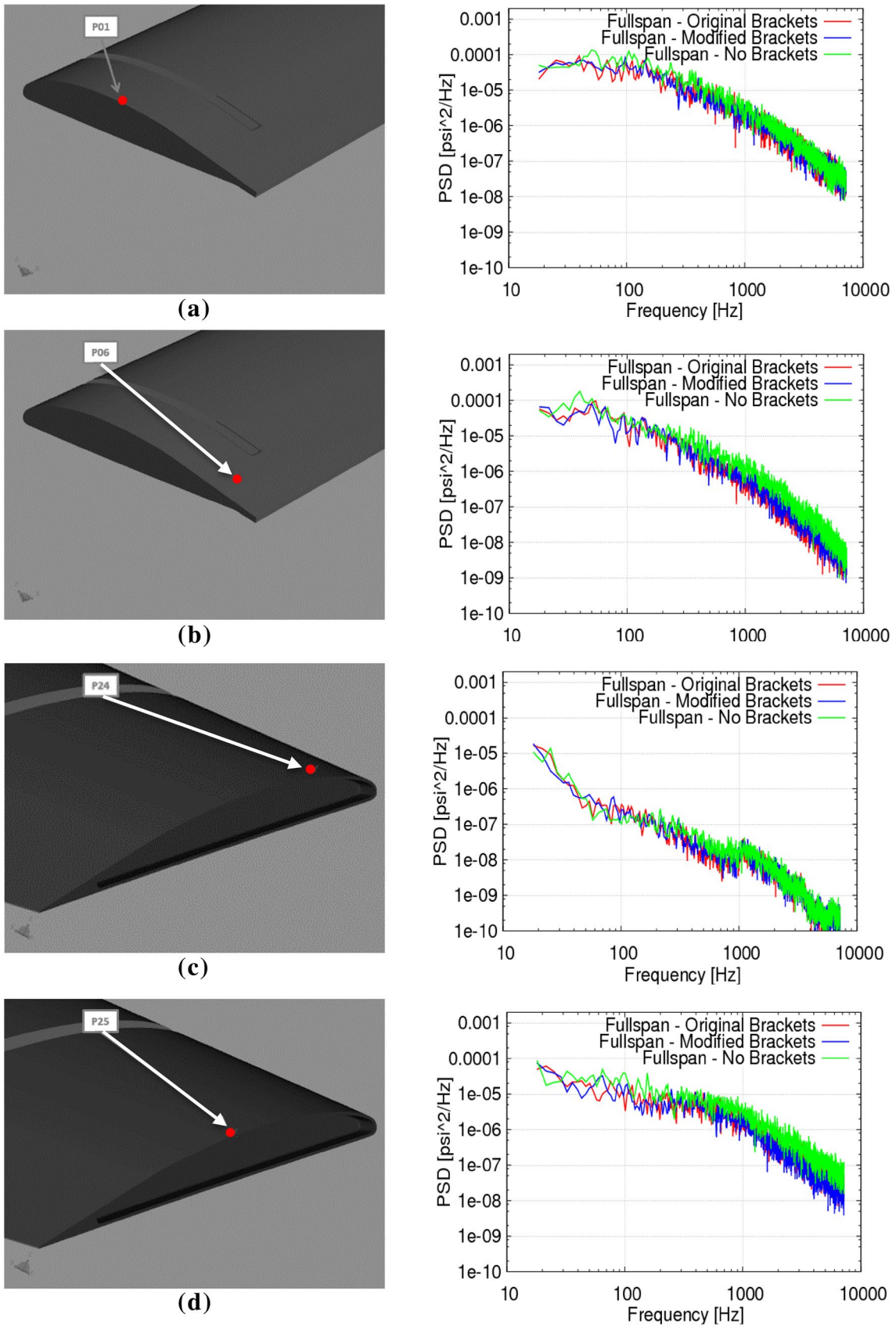
Fig. 43 Pressure spectra of surface probes on the flap side edges (from Ref. [23])
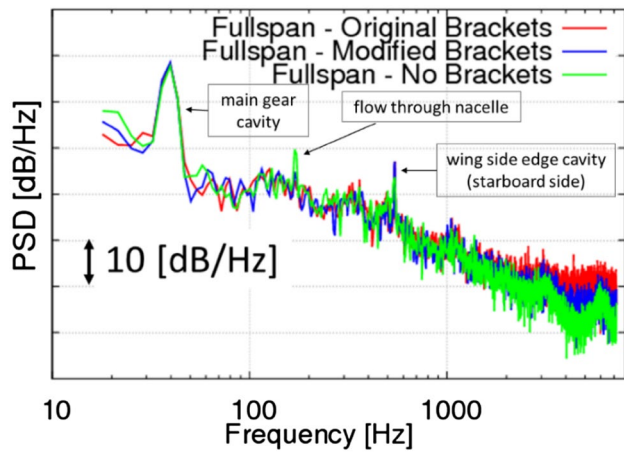
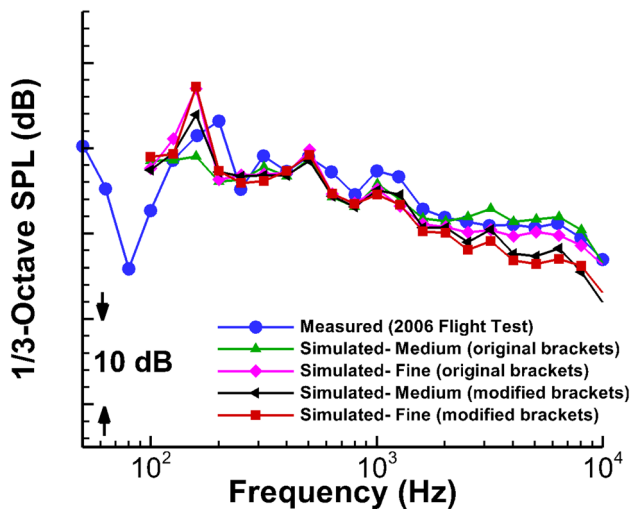**Fig. 44** Farfield pressure spectra at flyover microphone position (from Ref. [23])

Fig. 46 Farfield noise spectra for landing configuration with 39° flap deflection and main gear deployed. Computed spectra are based on FWH approach using pressure data on aircraft solid surfaces (from Ref. [30])

Fig. 45 Farfield noise spectra for landing configuration with 39° flap deflection and main gear retracted. Computed spectra are based on FWH approach using pressure data on aircraft solid surfaces (from Ref. [30])

Good correspondence between medium and fine mesh results was obtained, indicating that spatial resolution effects were adequately addressed even at the medium-resolution level and that, as expected, any lingering effects were mostly confined to the higher frequency range. Also, the agreement between predicted and measured SPLs was fairly good for frequencies up to 3 kHz. Beyond this frequency, differences emerged due to the increasing effect of bracket noise. Modification of the brackets seemed to improve agreement with measured levels at higher frequencies. Unfortunately, the latter simulation could not be repeated on the finest grid available before project conclusion to determine whether the close agreement attained could be extended to the highest frequencies of interest.
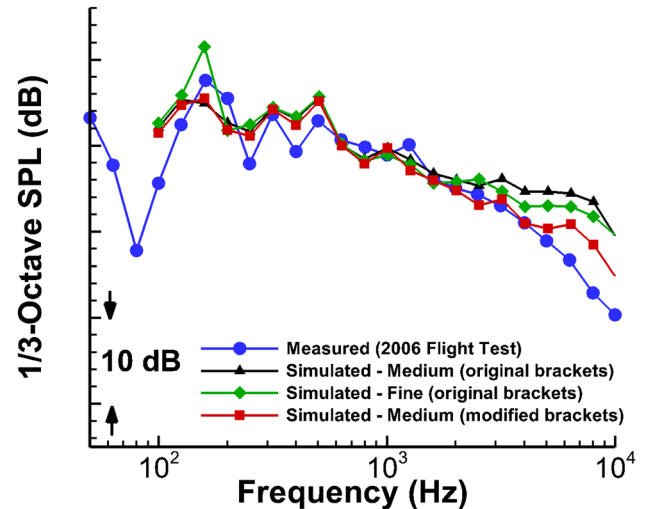
Simulation results were also validated using source localization (beamform) contour maps. Sample maps at two frequencies for the configuration with flaps deflected 39°, main gear deployed, and modified flap brackets are presented in Fig. 47 (from Ref. [30]). The contours have been normalized so that the peak SPL level in each map is zero. The axes give vehicle dimensions in feet. Both the experimentally measured flight-test data [19] and the simulated results used the same non-uniform, spiral cluster of 167 microphones that was deployed at the NASA Wallops Flight Facility for the 2006 flight test. To generate the maps from the computed data, the synthetic pressure record at each microphone location within the array was constructed using the pressures on the solid surfaces of the aircraft in a FWH propagation code. Array data processing and other details that enabled direct comparison between measured and computed beamform maps are provided in Ref. [30]. Figure 47a compares the contour maps from simulated and measured data for a frequency of 879 Hz. Very good agreement is observed, with both maps highlighting the flap tips and MLG as the prominent sound sources at this frequency. Due to limits in array resolution and the proximity of the main gear to the flap inboard edge, it was not possible to separate gear noise from the noise generated at the flap tip. Contour maps at 1270 Hz are presented in Fig. 47b. Good correspondence between simulated and measured data was achieved for this frequency as well. The flap outboard edge is the dominant noise source, and subsequent wind-tunnel testing [16] revealed the cause to be an interaction between the tip vortex and the bulb-seal cavity flow. At both frequencies, residual engine noise in the flight data is most likely causing the high levels in the region directly downstream of the wheels. Realizing that the maps
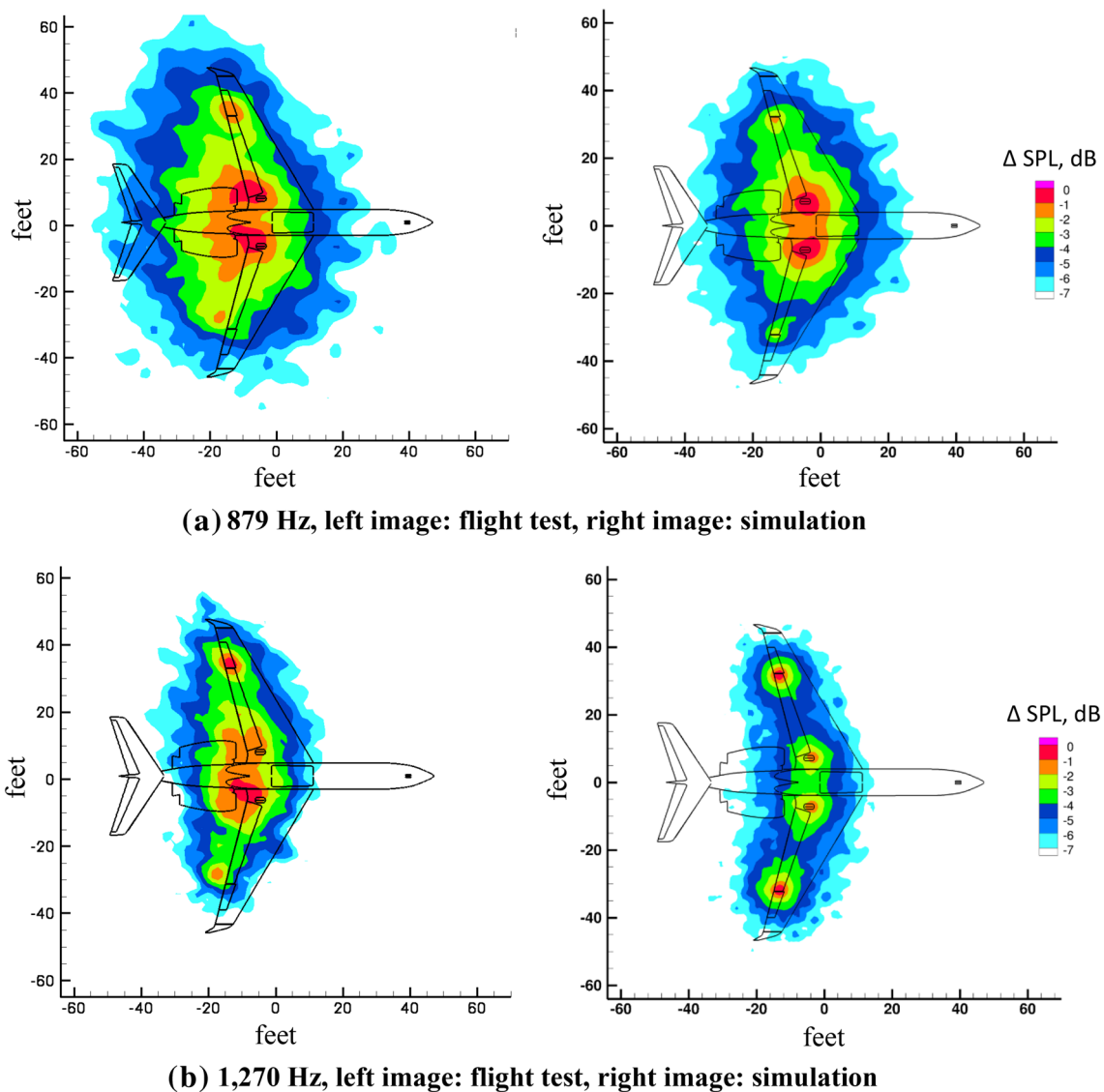
(a) 879 Hz, left image: flight test, right image: simulation

(b) 1,270 Hz, left image: flight test, right image: simulation

Fig. 47 Source localization (beamform) contour maps of SPL (in dB down from peak) for landing configuration with 39° flap deflection, main gear deployed, and modified brackets (from Ref. [30])

from the flight data correspond to a moving aircraft (source) with residual engine noise and uncontrolled meteorological conditions, whereas the present simulations are tailored to a stationary source without propulsion noise under controlled conditions, the agreement obtained at low-to-moderate frequencies is quite remarkable and very auspicious for the utility of future simulations.

Shortly before project conclusion, the computational approach was extended to include the nose landing gear (NLG), truly representing the complete, full-scale, landing aircraft geometry. As was the case for the MLG, the NLG model was developed from the original CAD geometry files furnished to NASA by the GAC and, therefore, includes all the finer details of the nose gear components as flown on the actual aircraft. The

computational procedure and the flow parameters (e.g., M, Re) for this configuration were the same as those used for the case with flaps deflected 39° and MLG deployed. The simulation for the full-scale, complete aircraft was successfully completed for the medium-resolution grid. Unfortunately, fine-resolution results could not be obtained prior to project conclusion.

Global images of the simulated vorticity field for the landing configuration of flaps deflected 39° and both MLG and NLG deployed are shown in Fig. 48. Note that the flow structures in the wake of the NLG and their downstream evolution are captured relatively well. As shown in Fig. 48a, the nose gear wake does not impact the flow fields associated with the MLG nor the inboard tip of the aircraft flaps. As depicted in Fig. 48b, most of the nose gear wake is

convected over the wing suction side near the root before the finer structures diminish and the larger structures start to diffuse. We note, however, that the wake's rapid loss of cohesiveness downstream of the wing leading edge may be due in part to insufficient spatial resolution in this area. Since contribution of volume sources to the farfield noise spectrum at low subsonic speeds is rather unimportant, except for those instances when significant component interaction is anticipated, downstream resolution of wakes far from the model solid surfaces had to be sacrificed to better manage computational resources and simulation costs.

Comparison of the predicted farfield noise spectrum with measurements from the 2006 flight test is shown in Fig. 49. Based on results from earlier computations (see Fig. 46), only the configuration with modified flap brackets was simulated. For the comparison to be meaningful, similar corrections as those described in Ref. [30] have been applied to the computed spectrum. Note from the figure that the predicted spectrum is in remarkable agreement with measured sound levels over the entire frequency range, indicating that airframe noise prediction of a full-scale, complete aircraft in landing configuration representative of a regional jet class of civil transports is within reach. Although valuable insight on the required grid resolution would have been available had we completed the finer resolution simulation, the information presented in Fig. 46 clearly indicates

that such a solution would have yielded results not dissimilar to the farfield spectrum obtained with the medium-resolution grid.
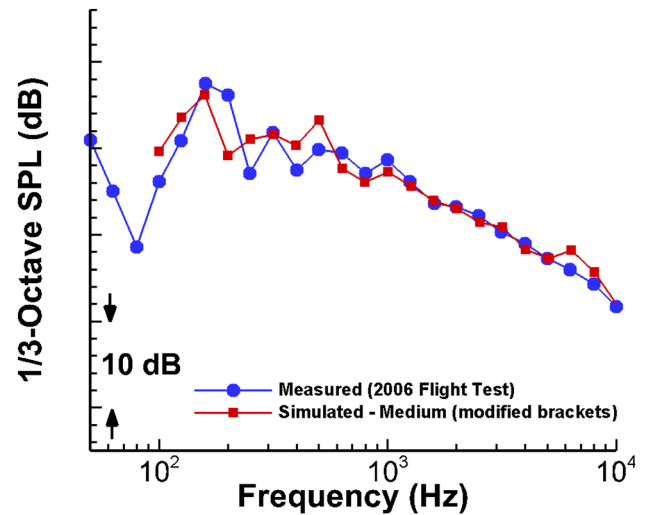

Fig. 49 Farfield noise spectra for landing configuration with 39° flap deflection and both nose and main gear deployed. Computed spectra are based on FWH approach that uses pressure data on aircraft solid surfaces

Fig. 48 Instantaneous vorticity field based on isosurface of λ_2 criterion for 39° flap deflection with both nose and main gears deployed

(a) Bottom view

(b) Side view
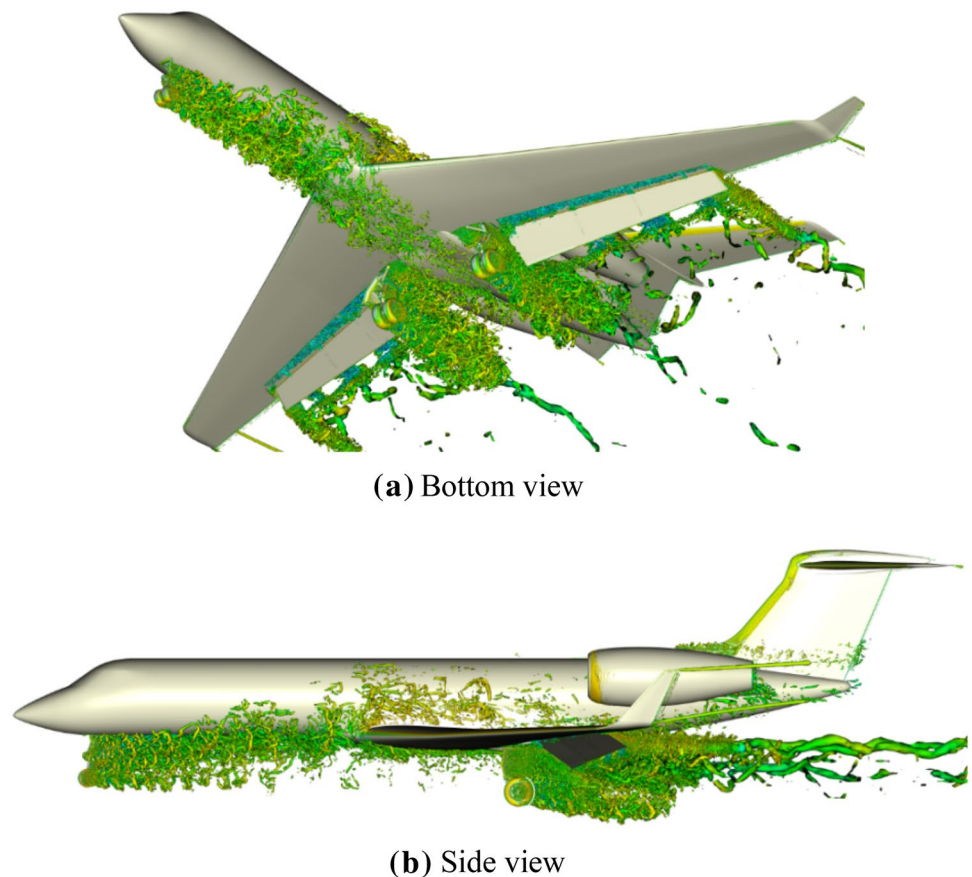
6 Summary

The present article provides an overview of extensive computational studies, executed during the 2011–2016 period, aimed at advancing simulation-based airframe noise prediction to include a full-scale, complete aircraft in landing configuration. To achieve this ambitious goal, an incremental, system-level approach to validate the predicted results and increase confidence in the selected computational methodology was undertaken. The computational effort was centered on conducting high-fidelity, time–accurate simulations, in model- and full-scale, of a Gulfstream aircraft that features nearly all of the finer details for the flap, main landing gear, and nose landing gear.

The Exa Corporation PowerFLOW® lattice Boltzmann based solver was used to perform the computations for free-air at $M = 0.2$. Extensive on- and off-surface flow measurements, combined with farfield acoustic data obtained for an 18%-scale, semispan model of the Gulfstream aircraft were used to fully validate the model-scale simulated results for two baseline landing configurations consisting of 39° flap deflection with and without the main landing gear deployed. The simulated on-surface time-averaged and fluctuating pressure fields on the model wing and flap were in excellent agreement with wind-tunnel measurements. Also, the simulated off-surface velocity field was in good agreement with PIV measurements. Most importantly, the predicted farfield spectrum for the 90° overhead position compared remarkably well with microphone array measurements. The model-scale noise prediction validation process was instrumental in attaining confidence in the selected computational methodology and its extension to the full-scale, complete aircraft during landing.

The full-scale simulations were conducted at $M = 0.2$ and $Re = 10.5 \times 10^6$, which is roughly half the flight Re (based on full-scale wing mean aerodynamic chord and aircraft landing speed). To ascertain solution convergence, the majority of the simulations were performed on three successively finer grids. Sample time-averaged and unsteady surface pressures on the flap, particularly near the side edges, were used to demonstrate the level of grid independence that was achieved. The results obtained from the full-scale simulations were validated using measured and predicted surface pressures of an 18%-scale version of the same aircraft, properly corrected for size. This approach was necessary because fully vetted flight-test data were not available. Overall, good correspondence between model- and full-scale surface pressures was observed. The most noticeable differences occurred at the flap outboard tip and were caused by a combination of Re effects and increased geometrical complexities of the tip cavity and bulb-seal assembly.

Farfield noise data from a 2006 flight test, acquired for three baseline configurations (flaps deflected 39° with and without main landing gear deployed, and flaps deflected 39° with nose and main gear deployed), were used to validate the computed solutions on medium and fine spatial resolution grids. With simulated spectra appropriately corrected to compensate for ground reflection effects present in the 2006 flight measurements, the broadband component of the computed farfield noise was in very good agreement with measured data for all three aircraft configurations considered. Most of the differences occurred at relatively high frequencies and were associated with higher uncertainties in the measured spectra and contributions from flap bracket noise. Sample source localization maps obtained from the simulated data for the configuration with flaps deflected 39°, main gear deployed, and modified flap brackets agreed well with corresponding maps from the 2006 flight test at low-to-moderate frequencies.

The full-scale computations presented here are the result of a first-time attempt to simulate the unsteady flow around a complete aircraft with high geometrical complexity. The success of the computational simulations resulted in a set of validated solutions that fostered the subsequent full-scale evaluation of several flap and main gear noise reduction concepts.

7 Future direction

The success of the present simulations in accurately predicting the complex, unsteady flow field around a complete aircraft and the resulting farfield noise signature has surpassed most of the original goals and milestones envisioned for the computational effort. When we began this work in early 2011, we did not anticipate that in six short years we would arrive at a stage whereby airframe noise prediction for a full-scale, regional jet in landing configuration is a reality rather than a distant goal. As remarkable as the current results may seem, we believe that we are just at the beginning of an arduous journey. The computational knowhow and experience gained thus far have provided the necessary confidence in the present computational approach to evaluate its suitability for an even more challenging problem. Work is progressing to advance the state-of-the-art in simulation-based airframe noise prediction methodologies. The effort, which is being performed under a collaboration between NASA and the Boeing Company, focuses on extending high-fidelity simulations to large civil transports (e.g., Boeing 777 or Airbus 330 class of aircraft). The complexities of the flow field and the size of these aircraft make achieving such simulations the "holy grail" of airframe noise prediction. Building upon the current experience, a series of steps have been developed that range from simulations of component-level, model scale

to full-scale, complete aircraft configurations. The complexities of the simulated geometry will be increased substantially at each step. Simulations of an isolated, high-fidelity, 26%-scale model of the B777-200 main landing gear with and without a noise reduction device have been completed. Initial comparisons of the predicted results with wind-tunnel measurements have been presented in Ref. [36]. The remarkable accuracy of the simulated farfield noise spectrum for the 26%-scale MLG and the predicted reduction in SPL achieved with the noise reduction device bode well toward extending the current methodology to the prediction of airframe noise for large civil transports. Nevertheless, we do not presume that success is assured. The challenges ahead are daunting. In our view, even setbacks along the way would be useful to gain insight into the shortcomings of the current computational tools and help advance the next stage of development.

References

1. Dobrzynski, W.: Almost 40 years of airframe noise research: what did we achieve. J. Aircraft. 47(2), 353–367 (2010)
2. Chalot, F., Mallet, M., Roge, G.: Review of recent developments and future challenges for the simulation-based design of aircraft. In: International Council of Aeronautical Sciences Paper ICAS 210-2.10.3 (2010)
3. Abbas-Bayoumi, A., Becker, K.: An industrial view on numerical simulation for aircraft aerodynamic design. J. Math. Ind. **1**, 10 (2011). https://doi.org/10.1186/2190-5983-1-10
4. Deck, S., Gand, F., Brunet, V., Ben Khelil, S.: High-fidelity simulations of unsteady civil aircraft aerodynamics: stakes and perspectives. Application of zonal detached eddy simulation. Philos. Trans. R. Soc. A (2014). https://doi.org/10.1098/rsta.2013.0325
5. Khorrami, M.R., Mineck, R.E.: Towards full-aircraft airframe noise prediction: detached eddy simulations. In: AIAA Paper 2014–2480 (2014)
6. Mineck, R.E., Khorrami, M.R.: On the importance of spatial resolution for flap side edge noise prediction. In: AIAA Paper 2017–3694 (2017)
7. Slotnick, J., Khodadoust, A., Alonso, J., Darmofal, D., Gropp, W., Lurie, E., Mavriplis, D.: CFD Vision 2030 study: a path to revolutionary computational aerosciences. NASA Contractor Report NASA/CR-2014-218178 (2014)
8. Seror, C., Sagaut, P., Blanger, A.: A numerical aeroacoustics analysis of a detailed landing gear. In: AIAA Paper 2004–2884 (2004)
9. Fares, E., Nölting, S.: Unsteady flow simulation of a high-lift configuration using a Lattice-Boltzmann approach. In: AIAA Paper 2011–0869 (2011)
10. Vatsa, V., Lockard, D.P., Khorrami, M.R., Carlson, J.-R.: Aeroacoustic simulation of a nose landing gear in an open-jet facility using FUN3D. In: AIAA Paper 2012–2280 (2012)
11. Casalino, D., Nölting, S., Fares, E., Vand de Ven, T., Perot, F., Bres, G.: Towards numerical aircraft noise certification: analysis of a full-scale landing gear in fly-over configuration. In: AIAA Paper 2012–2235 (2012)
12. Murayama, M., Yokokawa, Y., Imamura, T., Yamamoto, K., Ura, H., Hirai, T.: Numerical investigation on change of airframe noise by flap side-edge shape. In: AIAA Paper 2013–2067 (2013)
13. Bouvy, Q., Rougier, T., Ghouali, A., Casalino, D., Appelbaum, J., Kleinclaus, C.: Design of quieter landing gears through lattice-Boltzmann CFD simulations. In: AIAA Paper 2015–3259 (2015)
14. Khorrami, M.R., Hannon, J.A., Neuhart, D.H., Markowski, G.A., Van de Ven, T.: Aeroacoustic studies of a high-fidelity aircraft model: part 1—steady aerodynamic measurements. In: AIAA Paper 2012–2233 (2012)
15. Khorrami, M.R., Neuhart, D.H.: Aeroacoustic studies of a high-fidelity aircraft model: part 2- unsteady surface pressures. In: AIAA Paper 2012–2234 (2012)
16. Khorrami, M.R., Humphreys, W.M. Jr., Lockard, D.P., Ravetta, P.A.: Aeroacoustic evaluation of flap and landing gear noise reduction concepts. In: AIAA Paper 2014–2478 (2014)
17. Neuhart, D., Hannon, J., Khorrami, M.R.: Aerodynamic measurements of a gulfstream aircraft model with and without noise reduction concepts. In: AIAA Paper 2014–2477 (2014)
18. Yao, C.-S., Jenkins, L.N., Bartram, S.M., Harris, J., Khorrami, M.R., Mace, W.D.: Flow-field investigation of gear-flap interaction on a gulfstream aircraft model. In: AIAA Paper 2014–2479 (2014)
19. Khorrami, M.R., Lockard, D.P., Humphreys, W.M. Jr., Choudhari, M.M., Van de Ven, T.: Preliminary analysis of acoustic measurements from the NASA-gulfstream airframe noise flight test. In: AIAA Paper 2008–2814 (2008)
20. Khorrami, M.R., Humphreys, W.M. Jr., Lockard, D.P.: An assessment of flap and main landing gear noise abatement concepts. In: AIAA Paper 2015–2987 (2015)
21. Khorrami, M.R., Fares, E., Casalino, D.: Towards full-aircraft airframe noise prediction: lattice-Boltzmann simulations. In: AIAA Paper 2014–2481 (2014)
22. Fares, E., Casalino, D., Khorrami, M.R.: Evaluation of airframe noise reduction concepts via simulations using a lattice-Boltzmann approach. In: AIAA Paper 2015–2988 (2015)
23. Fares, E., Duda, B., Khorrami, M.R.: Airframe noise prediction of a full aircraft in model and full scale using a lattice Boltzmann approach. In: AIAA Paper 2016–2707 (2016)
24. Spalart, P.R., Deck, S., Shur, M.L., Squires, K.D., Strelets, M.K., Travin, A.: A new version of detached-eddy simulation, resistant to ambiguous grid densities. Theor. Comput. Fluid Dyn. **20**, 181–195 (2006)
25. Menter, F.R., Kuntz, M., Bender, R.: A scale adaptive simulation model for turbulent flow predictions. AIAA Paper 2003–0767 (2003)
26. Qian, Y., d'Humieres, D., Lallemand, P.: Lattice: BGK models for the Navier–Stokes equation. Europhys. Lett. **17**, 479–484 (1992)
27. Chen, H., Chen, S., Matthaeus, W.: Recovery of the Navier–Stokes equations using a lattice-gas boltzmann method. Phys. Rev. A **45**(8), 5339–5342 (1992)

28. Chen, S., Doolen, G.D.: Lattice Boltzmann method for fluid flows. Annu. Rev. Fluid Mech. **30**, 329–364 (1998)
29. Chen, H., Teixeira, C., Molvig, K.: Realization of fluid boundary conditions via discrete Boltzmann dynamics. Int. J. Mod. Phys. C **9**(8), 1281–1292 (1998)
30. Khorrami, M.R., Fares, E.: Simulation-based airframe noise prediction of a full-scale, full aircraft. In: AIAA Paper 2016–2706 (2016)
31. Khorrami, M.R., Fares, E., Duda, B., Hazir, A.: Computational evaluation of airframe noise reduction concepts at full scale. In: AIAA Paper 2016–2711 (2016)
32. Ffowcs Williams, J.E., Hawkings, D.L.: Sound generated by turbulence and surfaces in arbitrary motion. Philos Trans R Soc **A264**(1151), 321–342 (1969)
33. Farassat, F., Succi, G.P.: The prediction of helicopter discrete frequency noise. Vertica **7**(4), 309–320 (1983)
34. Najafi-Yazdi, A., Brès, G.A., Mongeau, L.: An acoustic analogy formulation for moving sources in uniformly moving media. Proc. R. Soc. Lond. A **467**(2125), 144–165 (2011)
35. Khorrami, M.R., Mineck, R.E., Yao, C.S., Jenkins, L.N.: A comparative study of simulated and measured gear-flap flow interaction. In: AIAA Paper 2015–2989 (2015)
36. Konig, B., Fares, E., Ravetta, P., Khorrami, M.R.: A comparative study of simulated and measured main landing gear noise for large civil transports. In: AIAA Paper 2017–3013 (2017)